PREPRINT（submitted to EESD）

Coupled structural and heat conduction FE analysis of laminated high damping rubber bearing

Tomoshi Miyamura *1, *3, Makoto Ohsaki *2, Jun Fujiwara*3, and Masashi Yamamoto *4
*1 Department of Computer Science, College of Engineering, Nihon University
1 Nakagawara, Tokusada, Tamura-machi, Koriyama 963-8642, Japan, miyamura@cs.ce.nihon-u.ac.jp
*2 Department of Architecture and Architectural Engineering, Graduate School of Engineering, Kyoto University, Kyoto, Japan
*3 National Research Institute for Earth Science and Disaster Resilience, Miki, Japan
*4 Earthquake Engineering Department, Takenaka R&D Institute, Takenaka Corporation, Tokyo, Japan

Abstract
A framework for coupled structural and heat conduction finite element analysis is developed for laminated high damping rubber bearings (HDRBs), and coupled analyses are conducted for full-scale tests of an HDRB using the shaking table at E-Defense. An HDRB, which is used in base-isolated buildings, is modeled using hexahedral solid elements. The high damping rubber is modeled as an overlaid visco-hyperelastic and elastic-plastic constitutive model. However, material parameters are identified using the results for the HDRB subjected to one-directional loading, and temperature dependences of the parameters are taken into account by a simple method based on empirical formulae for the HDRB because no cyclic coupon test was conducted for the high damping rubber used in the full-scale tests. The combined structural and heat conduction analyses are conducted for a number of loading cases. The same hexahedral mesh of the HDRB is used for both structural and heat conduction analyses. Analysis results are presented for a one-directional cyclic loading test, two-directional loading test with elliptical orbit, and earthquake loading test. The results obtained by the tests and those obtained by the coupled structural and heat conduction analyses are compared. The coupling effect of the mechanical and thermal behaviors is clearly shown in the analysis results, although reductions of the equivalent stiffness and damping are not large because the number of loading cycles in the present analyses is limited.

Keywords
Laminated high damping rubber bearing, Coupled structural and heat conduction finite element analysis, Visco-hyperelasticity, Elasto-plasticity, Energy dissipation, Full-scale test, E-Defense

1. Introduction

In countries with high seismic risk, base isolation is widely used for reducing seismic responses, mainly acceleration, of building frames by installing bearings and dampers at the base. Laminated rubber bearings are usually used for reducing horizontal responses by increasing the fundamental natural period, and accordingly, reducing the seismic energy input from the ground. The building can move easily in the lateral direction because laminated rubber bearings have small shear stiffness and capability of large shear deformation.

When natural rubber is used in laminated rubber bearings, vibration accompanied by large lateral deformation at the base-isolation layer should be reduced by attaching viscous dampers or hysteretic dampers using elastic-plastic deformation of a material such as steel or lead. A lead plug can also be inserted into the natural rubber bearing to dissipate energy by plastic deformation of the plug.

A laminated high damping rubber bearing (HDRB), which functions as both a bearing and damper, is often used in base isolation systems. The HDRB itself behaves as a damper, and therefore, the damping property can be obtained without a hysteretic or viscous damper. Many base-isolated buildings in Japan use only HDRBs without any additional dampers. In the past 5 years, however, oil dampers have been typically installed with HDRBs due to the experiences of the 2011 off the Pacific coast of Tohoku Earthquake of 9.0 Mw. Full-scale tests of an HDRB subjected to cyclic loading that realistically reproduced seismic acceleration [1] were conducted using the shaking table at the three-dimensional (3D) full-scale earthquake testing facility, E-Defense, at the Hyogo Earthquake Engineering Research Center of the National Research Institute for Earth Science and Disaster Resilience (NIED), Japan. These tests are referred to as E-Defense tests in the present paper. Coupled structural and heat conduction finite element (FE) analyses of the E-Defense tests of the HDRB using a mesh of solid elements are conducted in the present study.

The authors [2] investigated the basic properties of laminated natural rubber bearings using a hexahedral solid element mesh. Then, a 10-story reinforced concrete frame supported by two natural rubber bearings were modeled using hexahedral solid elements, and FE seismic response analyses of the base-isolated frame under severe earthquake ground motion were conducted to investigate deformation and the stress distribution. A parallel FE analysis package, ADVENTURECluster/E-Simulator [3, 4], was used for high-fidelity FE analysis. It has been shown that the local and global collapse behaviors of steel frames can be simultaneously simulated using high-fidelity FE analysis [5, 6].

Extensive research has been carried out for modeling mechanical properties and simulating large-deformation cyclic responses of laminated rubber bearings (e.g., [7]). A survey of previous work, including a number of studies

on HDRBs, which are also referred to in the present paper, can be found in Ref. [2]. Kelly and Konstantinidis [8] investigated the detailed behavior of rubber bearings, including buckling and friction, using analytical and numerical approaches. Constantinou et al. [9] reported a comprehensive description of current knowledge on the behavior of hardware used in seismic isolation and seismic damping systems. Analysis of a structural component composed of elastomeric material is very difficult because of its hyper-elastic property. Several material models have been presented for elastomers. In our previous study [2], the hyper-elastic constitutive relation for natural rubber was modeled using the Ogden model [10], which is more general than the Mooney-Rivlin model and the Neo-Hookean model [11]. Matsuda [12] developed a mixed displacement/pressure FE model for analysis of a natural rubber bearing under vertical pressure and shear, and extended it to a nonlinear viscoelastic model for an HDRB [13]. FE analysis was also carried out for natural rubber bearings in Refs. [14, 15].

Many studies can also be found for simulation of HDRBs. Abe et al. [16] combined elastoplastic and nonlinear elastic springs and a friction element for modeling HDRBs and natural rubber bearings. Yamamoto et al. [17] developed a two-dimensional model for HDRBs. Yoshida and Sugiyama [18] developed a visco-elastic-plastic model to simulate cyclic responses of an HDRB. Yuan et al. [19] carried out experiments to verify the one-dimensional constitutive relation for an HDRB. Mordini and Stauss [20] investigated the properties of bearings consisting of high-damping rubber and glass fiber layers. Das et al. [21] carried out a 3D FE analysis of fiber-reinforced rubber bearings to investigate the effect of the loading direction on the response under cyclic horizontal loads. The rubber material was represented by the Ogden model for hyper-elasticity and the Prony series for viscoelasticity.

Gracia et al. [22] developed an overlay model for simulating hyper-elastic and viscoelastic behavior. A rather simple viscoelastic model was used. Miehe and Keck [23] proposed a phenomenological material model by superimposing (overlaying) stresses due to elastic, elastoplastic, and viscoelastic materials. A similar superimposed or overlaid material model was also used in the present study; specifically the visco-hyperelastic material model proposed by Simo [24] and an elastic-plastic model with bilinear kinematic hardening were overlaid.

Many studies can be found on the temperature dependence of the mechanical properties of HDRBs and lead rubber bearings. Kalpakidis and Constantinou [25] derived an analytical formulation for the variation of the characteristic strength of a lead-rubber bearing under cyclic loading, and compared it with the experimental results [26]. Kalpakidis et al. [27] considered the effect of increased temperature on the mechanical properties of a lead rubber bearing. Cardone et al. [28, 29] experimentally investigated the effect of air temperature, including low temperature, on the mechanical properties of elastomers, such as shear stress at zero strain, maximum shear stress, secant shear modulus at the maximum stress, energy loss at each cycle, and equivalent viscous damping ratio. In Ref. [28], a number of 3D FE heat conduction analyses were conducted to investigate the thermal behavior of real (full-scale) steel-reinforced elastomeric isolators at low temperatures.

An important phenomenon in high damping rubber is the temperature rise caused by the energy dissipated due to inelastic strain during cyclic deformation. Therefore, the temperature rise and the mechanical behavior have an interaction, which means that a coupled structural and heat conduction analysis is necessary to precisely simulate the behavior of an HDRB. A number of studies on the coupled analysis of lead rubber bearings can be found. Kuroshima et al. [30] conducted a coupled analysis of a lead rubber bearing in which the structural behavior was analyzed by a mass-spring model, and the heat conduction was analyzed by a two-dimensional FE model. Yukawa et al. [31] conducted coupled heat and structural analyses and compared the results with their test results. Takenaka et al. [32] reported an experimental study on coupled heat and mechanical behavior of laminated HDRBs.

Only a few studies can be found for coupled analysis of HDRBs using elastomeric material [33]. This may be because the performance reduction for an HDRB subjected to a temperature rise due to the dissipated energy is small compared with that for lead bearings. In addition, a coupled FE structural analysis and FE heat conduction analysis has not been applied for investigating the properties of rubber bearings. Note that in many studies on coupled structural and heat conduction analyses of rubber bearings, a macroscopic model was used for the structural analysis.

The probability of an earthquake with a magnitude of 8–9 occurring within the next 30 years in the Nankai Trough area of Japan is estimated at 70–80% [34]. Such earthquakes, which are called the Great Nankai Trough Earthquakes, occur due to coupled ruptures at the tectonic plate boundary. Therefore, the duration of the coupled earthquakes is very long, and the earthquakes may excite strong long-period ground motion. NIED [35] simulated ground motions of earthquakes with a duration of 500 s. An HDRB in a base-isolated building with a natural period of 4 s experiences more than 100 cycles of deformation during these earthquakes. Although the long-duration cyclic tests of an HDRB conducted by Clark [36] suggested that the effect of temperature rise on mechanical properties is small, it is not negligible in a building subjected to earthquakes such as the Great Nankai Trough Earthquakes.

In the present paper, a framework is proposed for a coupled structural and transient heat conduction FE analysis of an HDRB, which is modeled using hexahedral solid elements. The following techniques are included

in the framework: material modeling of the high damping rubber and its material parameter identification, consideration of the temperature dependence of material parameters, and a numerical procedure for the coupled FE analysis. Then, the developed framework is applied to coupled structural and heat conduction FE analyses of the E-Defense tests of an HDRB.

The remainder of this paper is organized as follows. Section 2 provides an overview of the E-Defense tests. Section 3 outlines the formulation of the overlaid visco-hyperelastic and elastic-plastic constitutive model for high damping rubber, and describes techniques to consider the temperature dependence of the material parameters and material parameter identification. In Section 4, the computation procedure for the coupled structural and heat conduction FE analysis is described. Section 5 illustrates an analysis model for the HDRB. In Section 6, numerical results of the analyses are presented and compared to the results obtained by the E-Defense tests. Concluding remarks are given in Section 7.

2. Full-scale tests of a laminated high damping rubber bearing using the shaking table at E-Defense

A series of full-scale tests of an HDRB subjected to various cases of cyclic loading were conducted using the shaking table at E-Defense [1]. Figure 1 shows the specimen mounted in the test apparatus. Figure 2 shows the plans and elevation of the bearing. The locations of thermocouples are also shown in Figure 2. The number of rubber layers is 30, and the number of steel plate layers is 29. The rubber covering the circumferential surface is ignored. The diameter of the laminated circular rubber is 1,000 mm, the thickness of the rubber in each layer is 6.7 mm, and the thickness of the circular steel plate in each layer is 4.4 mm. The center of the HDRB has a hole with a diameter of 25 mm. Upper and lower steel flanges are attached to the outer rubber layers. The diameter and the thickness of the flanges are 1400 mm and 36 mm, respectively. A steel lower jig is located on the shaking table. Thirty-one load cells (three-component force sensors) are installed on the lower jig, and a thick plate is placed on the load cells. The HDRB test specimen is installed on the thick plate. Because the directions of the axes of load cells deviate from the X and Y axes in the test apparatus, the deviated measured values of load components are corrected to values in the X and Y directions.

The upper flange of the HDRB is fixed by a rigid frame that is rigidly supported on the floor of the test facility to provide the reaction force. An initial vertical pressure of 5 N/mm^2 is introduced by moving the shaking table in the upper direction. Various tests were conducted for only one specimen subjected to various lateral cyclic loadings with different patterns over 2 days. Tests subjecting the HDRB to one- or two-directional earthquake response wave loading, and two-directional loading with an elliptical orbit were conducted on the first day. After an interval of approximately 17 h, tests subjecting the HDRB to one-directional loading with a sinusoidal wave with a time-dependent amplitude, two-directional loading with a circular orbit, and large-amplitude loading were conducted on the second day. In the tests using one-directional loading and elliptical loading, 12 sets of cyclic loading were applied. Each loading set consisted of five cycles of cyclic loading with a period 4 s and an interval of 80 s between sets. In the present study, analyses are performed for the one-directional loading, the two-directional loading with an elliptical orbit (elliptical loading), and two-directional earthquake loading (hereafter, earthquake loading).

The material parameters used in the analyses are listed in Tables 1 to 3. Constitutive models, symbols in the tables, and parameter identification techniques are described in Section 3. One of the purposes of the E-Defense tests was to investigate the performance of an HDRB subjected to earthquake excitations of long duration and with long natural periods. The temperature increase of an HDRB subjected to excitations of the predicted Great Nankai Trough Earthquakes is estimated as follows. The volume of the elastomer used in the HDRB is calculated as 0.158 m^3 and its mass as 181 Kg. The heat capacity is 2.63×10^5 J/K. According to the discussion in Section 6, the external work for the hysteresis of the second cycle obtained by the one-directional loading test with a maximum shear strain of 200% is approximately 2.74×10^5 J, which corresponds to the area of the hysteresis loop shown in Figure 16 in Section 6. Therefore, the temperature rise per cycle is approximately 1 °C when a heat insulated boundary condition is assumed for the surfaces of the elastomer. It can be also calculated approximately using a formula to calculate temperature rise from the characteristic strength and the yield displacement, which was proposed in Ref. [9]. Finally, the total temperature rise in an HDRB in a base-isolated building subjected to long-period earthquakes is estimated as roughly 70 to 80 °C after more than 100 cycles, and its influence on the mechanical properties, such as the stiffness and damping capacity of the HDRB is significant.

3. Material models for high damping rubber

In the FE analyses, the HDRB is modeled with solid elements. The high damping rubber is modeled as an overlaid visco-hyperelastic and elastic-plastic constitutive model as shown in Figure 3. A similar superimposed or overlaid material model was proposed in Refs. [22, 23], although the temperature dependence of the material parameters was not taken into account. In the present study, the elastic-plastic constitutive model is a simple model using the isotropic hypo-elastic model, the von Mises yield criterion, and kinematic hardening with a

bilinear hardening curve. The visco-hyperelastic constitutive model is based on Simo's model [24], in which the Ogden hyper-elastic model and the two Maxwell models are combined.

Typical hysteresis loops in the load-displacement curves for different yield stresses are simulated using a rectangular coupon model described in Section 3.5. The material parameters for the HDRB shown in Table 1 are used for Case A. In contrast, the initial yield stress is taken to be almost zero for Case B; that is, all of the dissipated energy, specifically the area of the hysteresis loop, for Case B comes from the viscoelasticity. Figure 4 shows the hysteresis loops. The dissipated energy increases as the yield stress increases. The maximum load also increases as the yield stress increases, although the ratio of the change of the maximum load is smaller than that of the dissipated energy. Therefore, the equivalent damping factor depends greatly on the initial yield stress. The dissipated energy and the maximum load are also influenced by the change of the material parameters for the viscoelastic model and the change of loading speed.

The rest of this section provides an overview of the formulations of the visco-hyperelastic and elastic-plastic constitutive models used in the overlaid constitutive model, a method to overlay the two material models, a method to calculate the dissipated energy, a procedure for material parameter identification, and a simple method to account for the temperature dependence of the material parameters. The constitutive model is implemented in a parallel FE analysis package, ADVENTURECluster/E-Simulator [3, 4, 37]. The package ADVENTURECluster has been developed as a commercial code and has been verified and validated by solving various problems, including not only those related to civil and architectural structures but also problems in other fields, such as mechanical engineering. Its extended version, E-Simulator, has been applied to problems related to civil and architectural structures, and its verifications and validations have been continued [e.g., 2, 5, 6].

3.1 Visco-hyperelastic constitutive model

The visco-hyperelastic constitutive model is almost the same as Simo's model [24]. In the model, the Ogden hyper-elastic model and the two Maxwell models are combined in parallel. The strain energy density function of the Ogden model is defined as follows:

$$U = \sum_{n=1}^{2} \frac{\mu_n}{\alpha_n} (\bar{\lambda}_1^{\alpha_n} + \bar{\lambda}_2^{\alpha_n} + \bar{\lambda}_3^{\alpha_n} - 3) + K(J^{\beta} - 1)^{2\gamma}, \tag{1}$$

where K, α_1, α_2, μ_1, μ_2, β, and γ are material parameters. The variables $\bar{\lambda}_1$, $\bar{\lambda}_2$, and $\bar{\lambda}_3$ are the square roots of the principal values of the normalized left Cauchy–Green tensor $\bar{\boldsymbol{B}} = \bar{\boldsymbol{F}} \cdot \bar{\boldsymbol{F}}^{\mathrm{T}}$, and J is the volumetric deformation rate that is the determinant of the deformation gradient tensor $\boldsymbol{F}$. $\bar{\boldsymbol{F}} = J^{-1/3}\boldsymbol{F} \equiv (\det \boldsymbol{F})^{-1/3}\boldsymbol{F}$ is the normalized deformation gradient tensor. The initial shear modulus G is evaluated as $G = (\alpha_1\mu_1 + \alpha_2\mu_2)/2$. The instantaneous Kirchhoff tensor $\boldsymbol{T}_0(t)$ at time t is calculated by differentiating the function U by the principal invariants $\bar{I}_1$, $\bar{I}_2$, and $\bar{I}_3$ of $\bar{\boldsymbol{B}}$, and using the deformation gradient tensor as follows:

$$\boldsymbol{T}_0(t) = \boldsymbol{F}_0(t) \cdot \left\{ \left(\frac{\partial U(t)}{\partial \bar{I}_1} + \bar{I}_1(t) \frac{\partial U(t)}{\partial \bar{I}_2} \right) \bar{\boldsymbol{B}}(t) - \frac{\partial U(t)}{\partial \bar{I}_2} \bar{\boldsymbol{B}}(t) \cdot \bar{\boldsymbol{B}}(t) \right\} \cdot \boldsymbol{F}_0(t)^{\mathrm{T}}, \tag{2}$$

where $\boldsymbol{F}_0(t)$ is the deformation gradient tensor at time t with reference to the initial configuration.

Then, the Kirchhoff stress tensor $\boldsymbol{T}_{\mathrm{ve}}(t)$ for the viscoelastic constitutive model is calculated from the instantaneous Kirchhoff tensor $\boldsymbol{T}_0(t)$ by taking into account viscosity due to the Maxwell model. First, $\boldsymbol{T}_{\mathrm{ve}}(t)$ is decomposed into a deviatoric stress term $\boldsymbol{T}'(t)$ and a hydrostatic pressure term $\boldsymbol{T}^{\mathrm{V}}(t)$ as follows:

$$\boldsymbol{T}_{\mathrm{ve}}(t) = \boldsymbol{T}'(t) + \boldsymbol{T}^{\mathrm{V}}(t) \equiv \mathrm{dev}\left[\boldsymbol{T}_{\mathrm{ve}}(t)\right] + \frac{1}{3}\mathrm{tr}\left[\boldsymbol{T}_{\mathrm{ve}}(t)\right]\boldsymbol{I}, \tag{3}$$

where $\mathrm{tr}[\cdots]$ represents the sum of diagonal terms, $\boldsymbol{I}$ is the identity tensor, and $\mathrm{dev}[\cdots] = [\cdots] - 1/3\,\mathrm{tr}[\cdots]\boldsymbol{I}$. $\boldsymbol{T}'(t)$ and $\boldsymbol{T}^{\mathrm{V}}(t)$ are calculated from the deviatoric stress and hydrostatic pressure terms of $\boldsymbol{T}_0(t)$, which are denoted as $\boldsymbol{T}_0'(t)$ and $\boldsymbol{T}_0^{\mathrm{V}}(t)$, respectively, as follows:

$$\boldsymbol{T}'(t) = \boldsymbol{T}_0'(t) + \mathrm{dev}\left[\int_0^t \bar{\boldsymbol{F}}_t^{-1}(t-t') \cdot \dot{\gamma}(t') \boldsymbol{T}_0'(t-t') \cdot \bar{\boldsymbol{F}}_t^{-\mathrm{T}}(t-t')\,\mathrm{d}t' \right], \tag{4}$$

$$\boldsymbol{T}^{\mathrm{V}}(t) = \boldsymbol{T}_0^{\mathrm{V}}(t) + \int_0^t \dot{\kappa}(t') \boldsymbol{T}_0^{\mathrm{V}}(t-t')\,\mathrm{d}t', \tag{5}$$

where $\bar{\boldsymbol{F}}_t(t') = J_t(t')^{1/3}\boldsymbol{F}_t(t')$. $\boldsymbol{F}_t(t')$ and $J_t(t') = \det \bar{\boldsymbol{F}}_t(t')$ are the relative deformation gradient tensor and the volumetric deformation rate, respectively, at time t', with reference to the configuration at time t. The functions $\gamma(t)$ and $\kappa(t)$ are defined as follows:

$$\gamma(t) = 1 - \sum_{i=1}^{N} g_i \left(1 - e^{-t/t_i}\right), \tag{6}$$

$$\kappa(t) = 1 - \sum_{i=1}^{N} k_i \left(1 - e^{-t/t_i}\right), \tag{7}$$

where N is the number of the Maxwell models, t_i is the relaxation time, g_i is the dimensionless elastic shear modulus, and k_i is the dimensionless elastic bulk modulus. By differentiating $\gamma(t)$ and $\kappa(t)$ with respect to t, the following equations are obtained:

$$\dot{\gamma}(t) = -\sum_{i=1}^{N} \frac{g_i}{t_i} e^{-t/t_i}, \tag{8}$$

$$\dot{\kappa}(t) = -\sum_{i=1}^{N} \frac{k_i}{t_i} e^{-t/t_i}. \tag{9}$$

By substituting $\dot{\gamma}(t)$ in Equation (8) into Equation (4), the deviatoric stress term $\boldsymbol{T}'(t)$ is obtained as follows:

$$\boldsymbol{T}'(t) = \boldsymbol{T}_0'(t) - \sum_{i=1}^{N} \mathrm{dev}\left[\tilde{\boldsymbol{T}}_i(t)\right], \tag{10}$$

where

$$\tilde{\boldsymbol{T}}_i(t) = \frac{g_i}{t_i} \int_0^t e^{-t/t_i} \bar{\boldsymbol{F}}_t^{-1}(t-t') \cdot \boldsymbol{T}_0'(t-t') \cdot \bar{\boldsymbol{F}}_t^{-\mathrm{T}}(t-t') \,\mathrm{d}t'. \tag{11}$$

For the hydrostatic pressure term $\boldsymbol{T}^{\mathrm{V}}(t)$, the following equation is obtained by substituting $\dot{\kappa}(t)$ in Equation (9) into Equation (5):

$$\boldsymbol{T}^{\mathrm{V}}(t) = \boldsymbol{T}_0^{\mathrm{V}}(t) - \sum_{i=1}^{N} \tilde{\boldsymbol{T}}_i^{\mathrm{V}}(t), \tag{12}$$

where

$$\tilde{\boldsymbol{T}}_i^{\mathrm{V}} = \frac{k_i}{t_i} \int_0^t e^{-t/t_i} \boldsymbol{T}_0^{\mathrm{V}}(t-t') \,\mathrm{d}t'. \tag{13}$$

The Cauchy stress tensor $\boldsymbol{\sigma}_{\mathrm{ve}}(t)$ for the viscoelastic constitutive model is calculated from $\boldsymbol{T}'(t)$ and $\boldsymbol{T}^{\mathrm{V}}(t)$ as follows:

$$\boldsymbol{\sigma}_{\mathrm{ve}}(t) = \frac{1}{\det\left(\boldsymbol{F}_0(t)\right)}\left(\boldsymbol{T}'(t) + \boldsymbol{T}^{\mathrm{V}}(t)\right) \equiv \frac{1}{J_0(t)}\left(\boldsymbol{T}'(t) + \boldsymbol{T}^{\mathrm{V}}(t)\right). \tag{14}$$

3.2 Elastic-plastic constitutive model

The elastic-plastic constitutive model is based on the hypo-elastic model in rate form, that is, the hyper-elasticity is not considered in the elastic-plastic model. Deformation is described using the logarithmic strain tensor $\boldsymbol{\varepsilon}(t)$, which is calculated by integrating the deformation rate tensor $\boldsymbol{D}(t)$ as follows:

$$\boldsymbol{\varepsilon}(t) = \int_0^t \boldsymbol{D}(t) \,\mathrm{d}t. \tag{15}$$

The logarithmic strain tensor $\boldsymbol{\varepsilon}(t+\Delta t)$ at time $t+\Delta t$ is calculated approximately from $\boldsymbol{\varepsilon}(t)$ as follows:

$$\boldsymbol{\varepsilon}(t+\Delta t) = \boldsymbol{R}_t^{t+\Delta t} \cdot \boldsymbol{\varepsilon}(t) \cdot \boldsymbol{R}_{t+\Delta t}^{t} + \sum_{i=1}^{3}\left[\ln\left(\left(\lambda_i\right)_t^{t+\Delta t}\right)\left(\boldsymbol{v}_i\right)_t^{t+\Delta t} \otimes \left(\boldsymbol{v}_i\right)_t^{t+\Delta t}\right], \tag{16}$$

where $\boldsymbol{R}_t^{t+\Delta t}$ and $\boldsymbol{R}_{t+\Delta t}^{t}$ are orthogonal (finite rotation) tensors that represent the rotation from time t to time $t+\Delta t$ and that from time $t+\Delta t$ to time t, respectively. The orthogonal tensor is calculated from the axial vector of the spin tensor [38]. $\left(\lambda_i\right)_t^{t+\Delta t}$ and $\left(\boldsymbol{v}_i\right)_t^{t+\Delta t}$ ($i = 1 \sim 3$) are the eigenvalues (principal values) and the eigenvectors (principal directions) of the relative left stretch tensor $\boldsymbol{V}_t^{t+\Delta t}$ at time $t+\Delta t$ with reference to the configuration at time t. In the derivation of Equation (16), it is assumed that in the time interval between t and $t+\Delta t$, a rotation is followed by a deformation, and the principal directions of $\boldsymbol{V}_t^{t+\Delta t}$ do not change. The increment of the logarithmic strain tensor $\Delta\boldsymbol{\varepsilon}$ is calculated as follows:

$$\Delta\boldsymbol{\varepsilon} = \boldsymbol{\varepsilon}\left(t+\Delta t\right) - \boldsymbol{R}_{t}^{t+\Delta t}\cdot\boldsymbol{\varepsilon}\left(t\right)\cdot\boldsymbol{R}_{t+\Delta t}^{t} = \sum_{i=1}^{3}\left[\ln\left(\left(\lambda_i\right)_{t}^{t+\Delta t}\right)\left(\boldsymbol{v}_i\right)_{t}^{t+\Delta t}\otimes\left(\boldsymbol{v}_i\right)_{t}^{t+\Delta t}\right]. \tag{17}$$

The constitutive equation is defined for the deformation rate tensor $\boldsymbol{D}\left(t\right)$ and the Jaumann rate of the Cauchy stress tensor $\dot{\boldsymbol{\sigma}}^{(\mathrm{J})}\left(t\right)$ as follows:

$$\dot{\boldsymbol{\sigma}}^{(\mathrm{J})}\left(t\right) = \boldsymbol{C}^{\mathrm{e}} : \boldsymbol{D}^{\mathrm{e}}\left(t\right) \equiv \boldsymbol{C}^{\mathrm{e}} : \left(\boldsymbol{D}\left(t\right) - \boldsymbol{D}^{\mathrm{p}}\left(t\right)\right) \equiv \boldsymbol{C}^{\mathrm{ep}}\left(t\right) : \boldsymbol{D}\left(t\right), \tag{18}$$

where $\boldsymbol{C}^{\mathrm{e}}\left(t\right)$ is a fourth-order elastic constitutive tensor; $\boldsymbol{D}^{\mathrm{e}}\left(t\right)$ and $\boldsymbol{D}^{\mathrm{p}}\left(t\right) = \boldsymbol{D}\left(t\right) - \boldsymbol{D}^{\mathrm{e}}\left(t\right)$ are the elastic and plastic terms of $\boldsymbol{D}\left(t\right)$, respectively; and $\boldsymbol{C}^{\mathrm{ep}}\left(t\right)$ is a fourth-order elastic-plastic constitutive tensor. A simple elastic-plastic constitutive model with linear isotropic elasticity, the von Mises yield criterion, and a bilinear kinematic hardening is used in the present study.

The following stress tensor $\tilde{\boldsymbol{\sigma}}\left(t\right)$ observed in a co-rotational coordinate system for the contribution to the Cauchy stress tensor of the elastic-plastic model $\boldsymbol{\sigma}_{\mathrm{ep}}\left(t\right)$ is defined and used in the stress integration:

$$\tilde{\boldsymbol{\sigma}}\left(\tau\right) = \boldsymbol{R}_{\tau}^{t}\bullet\boldsymbol{\sigma}_{\mathrm{ep}}\left(\tau\right)\bullet\boldsymbol{R}_{t}^{\tau}, \tag{19}$$

where $\boldsymbol{R}_{\tau}^{t}$ and $\boldsymbol{R}_{t}^{\tau}$ are orthogonal tensors that represent the rotation from time τ to time t and that from time t to time τ, respectively. The rate form of Equation (19) is obtained by differentiating both sides of the equation with respect to t:

$$\dot{\tilde{\boldsymbol{\sigma}}}\left(t\right) = \boldsymbol{R}_{\tau}^{t}\bullet\dot{\boldsymbol{\sigma}}^{(\mathrm{J})}\left(\tau\right)\bullet\boldsymbol{R}_{t}^{\tau} = \boldsymbol{R}_{\tau}^{t}\bullet\left\{\dot{\boldsymbol{T}}^{(\mathrm{J})}\left(\tau\right) - \mathrm{tr}\left[\boldsymbol{D}\left(\tau\right)\right]\boldsymbol{\sigma}\left(\tau\right)\right\}\bullet\boldsymbol{R}_{t}^{\tau}, \tag{20}$$

where $\dot{\boldsymbol{\sigma}}^{(\mathrm{J})}\left(\tau\right)$ is the Jaumann rate of $\boldsymbol{\sigma}^{\mathrm{ep}}\left(\tau\right)$.

The stress tensor $\tilde{\boldsymbol{\sigma}}\left(t+\Delta t\right)$ is obtained from the following stress integration:

$$\tilde{\boldsymbol{\sigma}}\left(t+\Delta t\right) = \boldsymbol{\sigma}_{\mathrm{ep}}\left(t\right) + \int_{t}^{t+\Delta t}\dot{\tilde{\boldsymbol{\sigma}}}\left(\tau\right)\mathrm{d}\tau. \tag{21}$$

Equation (21) is rewritten by substituting Equations (20) and (18) into Equation (21):

$$\begin{aligned}\tilde{\boldsymbol{\sigma}}\left(t+\Delta t\right) &= \boldsymbol{\sigma}_{\mathrm{ep}}\left(t\right) + \int_{t}^{t+\Delta t}\boldsymbol{R}_{\tau}^{t}\bullet\left\{\boldsymbol{C}^{\mathrm{ep}}\left(\tau\right) : \boldsymbol{D}\left(\tau\right)\right\}\bullet\boldsymbol{R}_{t}^{\tau}\,\mathrm{d}\tau \\ &= \boldsymbol{\sigma}_{\mathrm{ep}}\left(t\right) + \int_{t}^{t+\Delta t}\boldsymbol{R}_{\tau}^{t}\bullet\left[\boldsymbol{C}^{\mathrm{e}} : \left\{\boldsymbol{D}\left(\tau\right) - \boldsymbol{D}^{\mathrm{p}}\left(\tau\right)\right\}\right]\bullet\boldsymbol{R}_{t}^{\tau}\,\mathrm{d}\tau\end{aligned}. \tag{22}$$

The integration in Equation (22) is conducted approximately by the backward Euler integration as follows [39]:

$$\tilde{\boldsymbol{\sigma}}\left(t+\Delta t\right) = \boldsymbol{\sigma}_{\mathrm{ep}}\left(t\right) + \boldsymbol{R}_{t+\Delta t}^{t}\bullet\left\{\boldsymbol{C}^{\mathrm{e}} : \left(\Delta\boldsymbol{\varepsilon} - \Delta\boldsymbol{\varepsilon}^{\mathrm{p}}\right)\right\}\bullet\boldsymbol{R}_{t}^{t+\Delta t}, \tag{23}$$

where $\Delta\boldsymbol{\varepsilon}$ is the increment of the logarithmic strain tensor $\boldsymbol{\varepsilon}\left(t\right)$ and $\Delta\boldsymbol{\varepsilon}^{\mathrm{p}}$ is the increment of plastic strain. Equation (23) is rewritten as

$$\boldsymbol{\sigma}_{\mathrm{ep}}\left(t+\Delta t\right) = \boldsymbol{R}_{t}^{t+\Delta t}\bullet\boldsymbol{\sigma}_{\mathrm{ep}}\left(t\right)\bullet\boldsymbol{R}_{t+\Delta t}^{t} + \boldsymbol{C}^{\mathrm{e}} : \left(\Delta\boldsymbol{\varepsilon} - \Delta\boldsymbol{\varepsilon}^{\mathrm{p}}\right), \tag{24}$$

and Equation (24) can be rewritten as

$$\boldsymbol{\sigma}_{\mathrm{ep}}\left(t+\Delta t\right) = \boldsymbol{C}^{\mathrm{e}} : \left(\boldsymbol{R}_{t}^{t+\Delta t}\bullet\boldsymbol{\varepsilon}^{\mathrm{e}}\left(t\right)\bullet\boldsymbol{R}_{t+\Delta t}^{t} + \Delta\boldsymbol{\varepsilon} - \Delta\boldsymbol{\varepsilon}^{\mathrm{p}}\right), \tag{25}$$

where $\boldsymbol{\varepsilon}^{\mathrm{e}}\left(t\right)$ is the total elastic strain tensor at time t. The increment of plastic strain $\Delta\boldsymbol{\varepsilon}^{\mathrm{p}}$ and the elastic-plastic constitutive tensor $\boldsymbol{C}^{\mathrm{ep}}\left(t+\Delta t\right)$, which is used to calculate the consistent tangent matrix, are obtained using the return mapping algorithm. Note that the logarithmic strain tensor and its increment are additively decomposed into elastic and plastic terms as the deformation rate tensor.

3.3 Stress integration and tangent stiffness

The Cauchy stress tensor $\boldsymbol{\sigma}$ for the overlaid visco-hyperelastic and elastic-plastic constitutive models is calculated using the following equation:

$$\boldsymbol{\sigma} = w_{\mathrm{ve}}\boldsymbol{\sigma}_{\mathrm{ve}} + w_{\mathrm{ep}}\boldsymbol{\sigma}_{\mathrm{ep}}\,, \tag{26}$$

where w_{ve} and w_{ep} are the weighted coefficients that satisfy

$$w_{\mathrm{ve}} + w_{\mathrm{ep}} = 1\,. \tag{27}$$

In the present study, both w_{ve} and w_{ep} are taken to be 0.5, and material parameters are identified for these coefficients. Because the materials in the overlaid model are connected in parallel, the strain tensors for the viscoelastic model and the elastic-plastic model are the same.

The stress at time $t+\Delta t$ is calculated by stress integration for each material model with respect to the increment of the displacement vector $\Delta\boldsymbol{u}$. The asymmetric tangent stiffness matrices that are consistent with the stress integration schemes are also derived. The tangent stiffness matrix for the entire system corresponds to the weighted sum of the tangent stiffness matrices using the weights w_{ve} and w_{ep}. The updated Lagrangian formulation is used. Note that the overlaid model can be implemented by simply overlaying two finite elements having the two constitutive models. In the present study, however, the two constitutive models are overlaid in an element using Equation (26).

3.4 Calculation of the dissipation and elastic energy of the overlaid model

The total dissipated energy density $W_{\mathrm{TotalDis}}(t)$ at time t is calculated as follows:

$$W_{\mathrm{TotalDis}}(t) = w_{\mathrm{ve}}\int_0^t J_o(t')\boldsymbol{\sigma}_{\mathrm{ve}}(t') : \dot{\boldsymbol{\varepsilon}}^{\mathrm{ve}}(t')\,dt' + w_{\mathrm{ep}}\int_0^t J_o(t')\boldsymbol{\sigma}_{\mathrm{ep}}(t') : \dot{\boldsymbol{\varepsilon}}^{\mathrm{p}}(t')\,dt'\,, \tag{28}$$

where $\dot{\boldsymbol{\varepsilon}}^{\mathrm{ve}}(t)$ and $\dot{\boldsymbol{\varepsilon}}^{\mathrm{p}}(t)$ are the velocities of an inelastic strain tensor due to the visco-hyperelastic deformation and a plastic strain tensor, respectively. The increment of W_{TotalDis}, denoted by $\Delta W_{\mathrm{TotalDis}}$, is calculated using the trapezoidal rule as follows:

$$\begin{aligned}
\Delta W_{\mathrm{TotalDis}} &= w_{\mathrm{ve}}\int_t^{t+\Delta t} J_o(t')\boldsymbol{\sigma}_{\mathrm{ve}}(t') : \dot{\boldsymbol{\varepsilon}}^{\mathrm{ve}}(t')\,dt' + w_{\mathrm{ep}}\int_t^{t+\Delta t} J_o(t')\boldsymbol{\sigma}_{\mathrm{ep}}(t') : \dot{\boldsymbol{\varepsilon}}^{\mathrm{p}}(t')\,dt' \\
&\approx w_{\mathrm{ve}}\frac{1}{2}\left(J_o(t+\Delta t)\boldsymbol{\sigma}_{\mathrm{ve}}(t+\Delta t) + J_o(t)\,\boldsymbol{R}_t^{t+\Delta t}\bullet\boldsymbol{\sigma}_{\mathrm{ve}}(t)\bullet\boldsymbol{R}_{t+\Delta t}^{t}\right) : \Delta\boldsymbol{\varepsilon}^{\mathrm{ve}} \\
&\quad + w_{\mathrm{ep}}\frac{1}{2}\left(J_o(t+\Delta t)\boldsymbol{\sigma}_{\mathrm{ep}}(t+\Delta t) + J_o(t)\,\boldsymbol{R}_t^{t+\Delta t}\bullet\boldsymbol{\sigma}_{\mathrm{ep}}(t)\bullet\boldsymbol{R}_{t+\Delta t}^{t}\right) : \Delta\boldsymbol{\varepsilon}^{\mathrm{p}}
\end{aligned}\,. \tag{29}$$

The increment of the plastic strain tensor $\Delta\boldsymbol{\varepsilon}^{\mathrm{p}}$ is obtained in the stress integration represented by Equation (25). However, the inelastic strain tensor $\boldsymbol{\varepsilon}^{\mathrm{ve}}(t)$ (viscoelastic strain) and its increment $\Delta\boldsymbol{\varepsilon}^{\mathrm{ve}}$ (increment of a viscoelastic strain) are not calculated explicitly in the formulation described in Section 3.1. Therefore, the viscoelastic strain is defined approximately only for calculating the dissipated energy based on the Maxwell model for the infinitesimal deformation. First the logarithmic strain tensor is decomposed into deviatoric and volumetric terms as follows:

$$\boldsymbol{\varepsilon}(t) = \boldsymbol{\varepsilon}'(t) + \boldsymbol{\varepsilon}^{\mathrm{V}}(t) \equiv \mathrm{dev}\left[\boldsymbol{\varepsilon}(t)\right] + \frac{1}{3}\mathrm{tr}\left[\boldsymbol{\varepsilon}(t)\right]\boldsymbol{I}\,. \tag{30}$$

Then, the viscoelastic strain is defined using Equations (6) and (7) as follows:

$$\boldsymbol{\varepsilon}^{\mathrm{ve}}(t) = \int_0^t \left(1-\gamma(t)\right)\frac{\mathrm{d}\boldsymbol{\varepsilon}'}{\mathrm{d}t'}\mathrm{d}t' + \int_0^t \left(1-\kappa(t)\right)\frac{\mathrm{d}\boldsymbol{\varepsilon}^{\mathrm{V}}}{\mathrm{d}t'}\mathrm{d}t'\,. \tag{31}$$

The increment of viscoelastic strain $\Delta\boldsymbol{\varepsilon}^{\mathrm{ve}}$ is calculated as

$$\Delta\boldsymbol{\varepsilon}^{\mathrm{ve}} = \boldsymbol{\varepsilon}^{\mathrm{ve}}(t+\Delta t) - \boldsymbol{\varepsilon}^{\mathrm{ve}}(t)\,. \tag{32}$$

The time derivatives of the strains are approximated using finite differences in the calculation of the time integrations in Equation (31).

Similarly, the elastic energy density $W_{\mathrm{TotalElas}}(t)$ for the overlaid model is defined as

$$W_{\mathrm{TotalElas}}(t) = w_{\mathrm{ve}}\int_0^t J_o(t')\boldsymbol{\sigma}_{\mathrm{ve}}(t') : {}^{\mathrm{e}}\dot{\boldsymbol{\varepsilon}}_{\mathrm{ve}}(t')\,dt' + w_{\mathrm{ep}}\int_0^t J_o(t')\boldsymbol{\sigma}_{\mathrm{ep}}(t') : {}^{\mathrm{e}}\dot{\boldsymbol{\varepsilon}}_{\mathrm{ep}}(t')\,dt'\,, \tag{33}$$

where ${}^{\mathrm{e}}\dot{\boldsymbol{\varepsilon}}_{\mathrm{ve}}(t)$ and ${}^{\mathrm{e}}\dot{\boldsymbol{\varepsilon}}_{\mathrm{ep}}(t)$ are the rates of the elastic strain tensors at time t for the visco-hyperelastic and elastic-plastic models, respectively. The increment of $W_{\mathrm{TotalElas}}(t)$ denoted by $\Delta W_{\mathrm{TotalElas}}$ is calculated using the trapezoidal rule in a manner similar to that in Equation (29) as follows:

$$\begin{aligned}\Delta W_{\text{TotalElas}} &= w_{\text{ve}}\int_t^{t+\Delta t} J_o(t')\boldsymbol{\sigma}_{\text{ve}}(t') : {}^{\text{e}}\dot{\boldsymbol{\varepsilon}}_{\text{ve}}(t')\,dt' + w_{\text{ep}}\int_t^{t+\Delta t} J_o(t')\boldsymbol{\sigma}_{\text{ep}}(t') : {}^{\text{e}}\dot{\boldsymbol{\varepsilon}}_{\text{ep}}(t')\,dt' \\ &\approx w_{\text{ve}}\frac{1}{2}\left(J_o(t+\Delta t)\boldsymbol{\sigma}_{\text{ve}}(t+\Delta t) + J_o(t)\boldsymbol{R}_t^{t+\Delta t}\bullet\boldsymbol{\sigma}_{\text{ve}}(t)\bullet\boldsymbol{R}_{t+\Delta t}^{t}\right) : \Delta^{\text{e}}\boldsymbol{\varepsilon}_{\text{ve}} \\ &+ w_{\text{ep}}\frac{1}{2}\left(J_o(t+\Delta t)\boldsymbol{\sigma}_{\text{ep}}(t+\Delta t) + J_o(t)\boldsymbol{R}_t^{t+\Delta t}\bullet\boldsymbol{\sigma}_{\text{ep}}(t)\bullet\boldsymbol{R}_{t+\Delta t}^{t}\right) : \Delta^{\text{e}}\boldsymbol{\varepsilon}_{\text{ep}}\end{aligned} \quad . \tag{34}$$

The increments $\Delta^{\text{e}}\boldsymbol{\varepsilon}_{\text{ve}}$ and $\Delta^{\text{e}}\boldsymbol{\varepsilon}_{\text{ep}}$ are calculated from $\Delta\boldsymbol{\varepsilon}^{\text{ve}}$ and $\Delta\boldsymbol{\varepsilon}^{\text{p}}$ as follows:

$$\Delta^{\text{e}}\boldsymbol{\varepsilon}_{\text{ve}} = \Delta\boldsymbol{\varepsilon} - \Delta\boldsymbol{\varepsilon}^{\text{ve}}, \tag{35}$$

$$\Delta^{\text{e}}\boldsymbol{\varepsilon}_{\text{ep}} = \Delta\boldsymbol{\varepsilon} - \Delta\boldsymbol{\varepsilon}^{\text{p}}. \tag{36}$$

Finally, the total dissipated energy and the elastic energy are obtained by the volumetric integration of $W_{\text{TotalDis}}(t)$ and $W_{\text{TotalElas}}(t)$, respectively, in the initial configuration.

3.5 Parameter identification using one-directional loading test

A material parameter identification tool combining simulated annealing and the E-Simulator is developed. However, cyclic coupon test was not conducted in the previous study [1] for the high damping rubber used in the E-Defense tests. In the present study, material parameters are identified approximately and tentatively using the result for the second and the third cycles of the one-directional loading test of the bearing. As a result, the present parameter identification becomes a calibration to reproduce the results of the one-directional loading test. As described in Section 6, the hysteresis for the first cycle exhibits unscragged characteristics. The rubber recovered its virgin properties 17 h after the tests performed during the previous day. The unscragged behavior is not simulated in the present study because the large dissipated energy during the first cycle becomes negligible after the dissipation energies for many cycles in the scragged state are accumulated. The identified parameter values are considered to exist at 30 °C, which corresponds to the initial temperatures measured by thermocouples inserted in the rubber, as described in Section 6.3, although there are some differences in the measured temperatures at different points. The rubber did not cool down to room temperature after 17 h. Temperature dependences of material parameters are taken into account by referring to empirical formulae proposed in Ref. [1] for the HDRB used in the E-Defense tests, as described in Section 3.6.

In the one-directional loading test, the shear deformation of each layer of rubber can be assumed to be homogeneous except for the peripheral region. Therefore, a rectangular coupon model that approximates the deformation of one layer of rubber of the HDRB is used for the parametric analyses in the parameter identification process. The mesh of the model is shown in Figure 5. The model contains only one rubber layer, which is shown in blue, and two steel layers, which are shown in green. All nodes on the upper surface of the upper flange are connected to a control node that is placed in the center of the upper surface using rigid beam elements that are represented using sets of multi-point constraints. The bottom face of the lower steel layer is fixed.

A vertical compressive pressure of 5 MPa is applied to the upper face of the upper steel layer by applying a nodal load to the control node. Then, the lateral cyclic displacement, which reproduces the same nominal shear strain as that of the HDRB model, is prescribed at the control node. The nominal shear strain of rubber is defined as the lateral displacement divided by the sum of the heights of the rubber layers, which is $6.7\times 30 = 201$ mm for the HDRB model, and the height of a rubber layer of the rectangular coupon model is 4 mm. The maximum shear strain is 200%. The nominal shear stress is defined as the lateral load divided by the initial area of a rubber layer.

The error between the nominal shear strain-stress curves obtained by the FE analysis using the rectangular coupon model and by the E-Defense tests of the HDRB is minimized by solving an optimization problem. This problem identifies the parameters for the viscoelastic constitutive model, that is, α_1, α_2, and relaxation times t_1 and t_2 for Maxwell models 1 and 2, and the parameters for the elastic-plastic constitutive model, specifically Young's modulus and the initial yield stress. The variable parameters in the optimization process are surrounded by boxes in Tables 1 and 2. The selection of these variable parameters may need further investigation. Simulated annealing, a heuristic approach [40], is used because the optimization problem is highly nonlinear, and many local optimal solutions may exist. A tool combining simulated annealing and the E-Simulator is developed for finding the parameter set minimizing the error. Details of simulated annealing can be found in Ref. [40]. The hardening coefficient is taken to be 1/1000 of the Young's modulus. The identified material parameters are shown in Tables 1 and 2. The catalog values or the values measured in the experimental study [1] are used for other material parameters.

3.6 Consideration of temperature dependence

The temperature dependences of the material parameters in both the elastic-plastic and viscoelastic models

influence the changes of the stiffness and the dissipated energy. If various cyclic coupon tests of the rubber subjected to different loading speeds at different temperatures are conducted and various load-displacement curves are available, the material parameters for both the viscoelastic and the elastoplastic models at different temperatures can be identified using the technique described in Section 3.5. Such load-displacement curves, however, have not previously been obtained for the rubber used in the HDRB. In the present study, the temperature dependences are considered by referring to the empirical formulae [1] for the equivalent stiffness and the equivalent damping factor for the HDRB. The formulae were derived in Ref. [1] from the results of the E-Defense tests and those of the preliminary test using a 1/4 scale model. In this study, the material parameters at 30 °C identified in Section 3.5 is modified by using temperature-dependent factors based on the formulae.

The empirical formula for the equivalent shear stiffness $k_{eq}(T)$ at temperature T (°C) is as follows:

$$k_{eq}(T) = C_K(T)\,k_{eq}(20), \tag{37}$$

where

$$C_K(T) = \begin{cases} 1.0 - 0.0144(T-20) & (T \le 20\ ^\circ\mathrm{C}) \\ 1.0 + 0.548\left\{\log_{10}(20-3.45) - \log_{10}(T-3.45)\right\} & (T > 20\ ^\circ\mathrm{C}) \end{cases}. \tag{38}$$

The empirical formula for the equivalent damping factor $h_{eq}(T)$ at temperature T is represented as follows:

$$h_{eq}(T) = C_H(T)\,h_{eq}(20), \tag{39}$$

where

$$C_H(T) = 1.0 - 0.0065(T-20). \tag{40}$$

The temperature dependences of the material parameters are determined to reproduce the relation for $k_{eq}(T)$ and $h_{eq}(T)$ in Equations (37) and (39), respectively, which are macroscopic values that represent the structural response of the entire HDRB.

The temperature dependences of Young's modulus $E(T)$ for the elastic-plastic model, shear parameters for the Ogden model $\mu_i(T)$ $(i=1,2)$, and shear moduli in the Prony series of the Maxwell model $g_i(T)$ $(i=1,2)$ are represented by multiplying the coefficient $C_K(T)$ by the parameters at 20 °C as follows:

$$E(T) = E(20)C_K(T), \tag{41}$$

$$\mu_i(T) = \mu_i(20)C_K(T) \quad (i=1,2), \tag{42}$$

$$g_i(T) = g_i(20)C_K(T) \quad (i=1,2). \tag{43}$$

The equivalent damping factor, h_{eq}, is calculated as follows:

$$h_{eq} = \frac{1}{4\pi}\frac{\Delta W}{W}, \tag{44}$$

where ΔW is the dissipated energy (energy absorption) measured as the area of the hysteresis loop and W is the maximum strain energy that corresponds to the area of the triangle in Figure 6.

Here, the temperature dependence of the equivalent damping factor is assumed to be represented only by changing the yield stress. The parameters for the visco-hyperelastic model are assumed to be constant. In Figure 4 it is understood that the amount of energy dissipation depends on the initial yield stress. In contrast, the change in the maximum load due to the change in the initial yield stress is rather small, which means that the change in W is smaller than the change in ΔW. Therefore, the equivalent damping factor h_{eq} can be controlled by the value of the initial yield stress.

A preliminary parametric study is conducted using the rectangular coupon model in Figure 5 subjected to one-directional loading, and the values obtained by Equation (39) for the results of the analyses are compared with the results of the E-Defense tests. The results of the numerical analysis using the parameters in Tables 1 to 3 show that the percentage of the contribution of the elastic-plastic model to the entire dissipated energy obtained by the overlaid model at 30 °C is approximately between 20% and 30%, which depends on the load amplitude. According to Equation (40), $C_H(60) = 0.74 = 74\%$, and this percentage can be represented by taking the yield stress to be almost zero at 60 °C. In other words, if the contribution of the elastic-plastic model becomes almost zero at 60 °C, the entire energy dissipation per cycle at 60 °C becomes between 70 and 80% of that at 30 °C.

According to the above discussion, the temperature dependence of the yield stress is given as follows:

$$\sigma_y(T) = \alpha(T)\,\sigma_y(20), \tag{45}$$

where $\sigma_y(T)$ is the yield stress at temperature T and $\alpha(T)$ is the following function of T:

$$\alpha(T)=\begin{cases}1 & (T\le 20)\\ 1.0-\dfrac{0.99}{40}(T-20) & (20<T<60)\\ 0.01 & (60\le T)\end{cases}. \tag{46}$$

Equation (46) results in an almost constant equivalent damping factor when T is more than 60 °C.

FE analyses are conducted using the rectangular coupon model for a number of constant temperatures. The hysteresis loops for the load-displacement curves are shown in Figure 7, and the equivalent damping factors are calculated and shown in Table 4. It is confirmed that the calculated dissipated energy is approximately the same as the external work computed from the area of the hysteresis loop. In Table 4, the equivalent damping factors evaluated by the FE analyses using Equation (44) are compared with those calculated using the empirical formula in Equation (39), and the differences in percentage are also shown. The damping factors obtained by the FE analyses agree well with those obtained by the empirical formula. In the following analyses of the HDRB, Equations. (41)–(43), (45), and (46) are used. Note that the material parameters at 20 °C are first calculated from those at 30 °C using these equations because the factors in these equations are calculated with respect to the reference value at 20 °C.

The method described in this section is not a general method. Equation (46) is only based on the observation of the dissipated energy obtained by the one-directional loading test. The material parameters are also identified approximately using only the results of the one-directional loading test. The contribution of the viscoelastic model to the dissipated energy may change in other loading cases, and the temperature dependences of the viscoelastic properties have to be considered. In addition, there is a limitation that the decrease of the equivalent damping factor cannot be represented when the temperature increases beyond 60 °C. The coupon tests at various loading speeds and temperatures will be conducted and the approximate method presented in this section will be replaced by the material parameter identifications at the different temperatures and interpolations of the identified parameters in a future study. In this approach, sets of parameters at different temperatures are obtained and they can be interpolated. Then, a set of material parameters at an arbitrary temperature can be calculated.

4. Coupled structural and heat conduction analysis

The schematic flow of the coupled analysis is shown in Figure 8. A weak coupling method is adopted, that is, the structural analysis and the heat conduction analysis are conducted in a staggered manner. Heat generation due to the dissipated energy from the viscoelastic model and the elastic-plastic model is calculated in the structural FE analysis, and it is applied as internal heat generation. Then, the temperature field is calculated in the transient heat conduction FE analysis. After obtaining the temperature field, mechanical material parameters are updated at each integration point of elements using the equations described in Section 3.6. Then, the structural analysis is conducted. Note that the same FE mesh is used in both the structural and heat conduction analyses.

5. Analysis model

In Ref. [2], the mesh for a laminated rubber bearing was generated using eight-node linear hexahedral solid elements for the simulation of the laminated natural rubber bearing. The mesh for the present study is made by modifying the mesh from the previous study. Figure 9 (a)-(d) shows the mesh of the HDRB shown in Figure 2. The same mesh, consisting of eight-node hexahedral elements, is used for both the structural and the heat conduction analyses. In the structural analysis, a fully integrated linear element is used for rubber, and a hexahedral element using linear interpolation functions enhanced by incompatible modes [41] is used for steel. The element behaves like a higher order element. In the heat conduction analysis, a fully integrated linear element is used.

For the structural analysis, two analysis models with different boundary conditions are compared in preliminary analyses. One analysis model is called the *control node model*, which has boundary conditions similar to those for the rectangular coupon model in Figure 5. All nodes on the lower surface of the lower flange are fixed. All nodes on the upper surface of the upper flange are connected to a control node that is placed at the center of the upper surface using rigid beam elements, as shown in Figure 9 (a). The rotations at the control node are fixed. The history of the sum of the measured vertical load is first assigned to the control node and applied as a nodal time-dependent load. The vertical load fluctuated due to the lateral deformation. The vertical load at the first time step is applied incrementally without considering the viscosity and plasticity of rubber. The initial vertical compressive pressure applied to the upper face of the upper steel layer is approximately 5 MPa. Histories of the measured lateral displacements are next assigned to the control node and prescribed as nodal time-dependent displacements. The mass (self-weight) of the HDRB is considered in all processes.

The other analysis model is called the *load cell model*, which directly applies the histories of vertical loads measured by the load cells, whose locations are shown in Figure 10(a). The thick plate attached under the lower

flange is also discretized as an FE mesh. All nodes on the lower surface of the thick plate are fixed in both horizontal directions. Load cells are modeled using four segments of the surface patch of the mesh of the thick plate, as shown in Figure 10(b). A control node, which is the same as the control node in the control node model, is placed on the upper surface of the upper flange. The vertical displacement and the rotations at the control node are fixed. The measured histories of vertical loads are applied as vertical pressure to the segments that model the load cells. The vertical loads at the first time step are applied incrementally without considering the viscosity and plasticity of rubber. The measured lateral displacements of the histories are also assigned to the control node and prescribed as nodal time-dependent displacements. In this model, the eccentricity of the distribution of the vertical load due to deformation and rattling of the jig is corrected automatically. However, fluctuations and noise in the measured data are also applied.

Static incremental analyses using the two analysis models are conducted for both the vertical and lateral loadings. The vertical loading is applied in 6 incremental steps, and the lateral loading of one cycle is applied in 20 steps, that is, the time for one cycle is 4 s and the time increment is 0.2 s. Although the function of an automatic increment control is used, the width of an increment is not reduced in the computation for each cycle.

According to the results of the preliminary analyses, the load-cell model leads to a load-displacement curve slightly closer to the test result than does the control node model. However, the difference between the results for the two models is very small. The computational time for the load cell model is longer than that for the control node model because the convergence of the iterative linear solver becomes worse for the load cell model. Therefore, the control node model is adopted for subsequent analyses.

For the heat conduction analysis, heat transfer boundary conditions are set for all surfaces of the model, and the coefficient of heat transfer is set as 0.01 mW/(mm^2 K). Two differences exist between the analysis model and the real specimen in the setting of heat conditions: (1) the outside air temperature is taken to be 30 °C, which is higher than the actual temperature, and (2) heat insulated boundary conditions are not set for the insulation sheets that are attached to the upper surface of the upper flange and the lower surface of the lower flange. Re-computations using corrected conditions are not conducted because computational resources were limited. They should be taken into account in future research. According to the temperature contours shown in Figure 14, a lower temperature due to the lack of heat insulation can be observed only in one layer of rubber.

The total numbers of nodes and solid elements in the control node model are 585,061 and 564,384, respectively. The number of rigid beams is 6,217. The number of degrees of freedom, including those of the rigid beams and the control node, is 1,773,834

6. Numerical results

Combined structural and transient heat conduction FE analyses are conducted for one-directional loading, elliptical loading, and earthquake loading. The schedule for these loadings is described in Section 2. Both mechanical and thermal responses are visualized, and the results are compared with those obtained by the E-Defense tests. The locations of thermocouples in the test specimen are shown in Figure 2. The time histories of temperature obtained by thermocouples at points A1, B1, C2, and C3 during the tests and the numerical analyses are compared

The accumulated external work is equal to the sum of the accumulated dissipated energy and the accumulated elastic energy related to residual stress. Because the dissipated energy is much larger than the elastic energy in the HDRB, the dissipated energy can be approximately evaluated by the external work, which is calculated from the measured time histories of the total lateral load and the lateral displacements at the top of the upper flange using the following equation for the increment of the external work:

$$\Delta W_{\text{External}}\left(t\right)=\frac{1}{2}\left(\boldsymbol{U}^{t+\Delta t}-\boldsymbol{U}^{t}\right)\cdot\left(\boldsymbol{P}^{t+\Delta t}+\boldsymbol{P}^{t}\right), \tag{47}$$

where $\boldsymbol{U}^{t}$ is the measured displacement vector at time t at the center of the upper surface of the upper flange and $\boldsymbol{P}^{t}$ is the measured load vector at time t. The external work for a time interval $\left[t_a,t_b\right]$ is calculated by summing the increments in Equation (47) as follows:

$$W_{\text{External}}\left(t_b\right)-W_{\text{External}}\left(t_a\right)=\sum_{i=0}^{n-1}\Delta W_{\text{External}}\left(t_i\right), \tag{48}$$

where $t_i=t_a+i\Delta t$ and $t_b=t_a+n\Delta t$. The external energy for one cycle of the hysteresis loop calculated using Equation (48) corresponds to the area of the hysteresis loop. The external energy is also calculated in the FE analysis by applying Equations (47) and (48) to all the nodal displacement vectors and the nodal equivalent force vectors and summing the nodal contributions.

In the one-directional loading and the elliptical loading cases of the E-Defense tests, 12 sets of cyclic loading are applied. Each set consists of five cycles of loading with a period of 4 s and an interval of 80 s between sets as described in Section 2. In the one-directional loading case, the cyclic load is controlled to achieve a sinusoidal displacement history at a loading point, which is shown in Figure 11. In the elliptical loading case, the cyclic load

is controlled to trace an elliptical orbit as shown in Figure 12. The lateral displacement history in the longer axis at the top of the upper flange is almost the same as that shown in Figure 11 for the one-directional loading except for that of the initial cycle.

Only six sets of cyclic loading are applied in both cases due to computational resource limits, and the limitation of the approximate method using Equations (45) and (46) for consideration of the temperature dependence of the dissipated energy of rubber, which can only be applied to temperatures less than 60 °C, as described in Section 3.6. Note that the maximum temperature observed at point C2 in the 12th loading set of the one-directional loading test is approximately 60 °C, and that of the elliptic loading test is 74 °C.

6.1 Results for one-directional loading

Figure 13 shows the deformation and contours of the equivalent stress at one time step during the last loading cycle of the 6th set of loading when the lateral displacement at the control node has the maximum value. Figures 13(a) and 13(b) show the overall and close-up views, respectively. In the middle layers of the HDRB, almost homogeneous shear deformation is observed. Some stress concentration and vertical deformation are observed in the regions around the left side of the upper layers and the right side of the lower layers. Figure 14 shows cross-sectional views of the temperature contours at the last time step indicated in Figure 11. Figures 14(a) and 14(b) show the entire and close-up views, respectively. The maximum sheer strain is 200%. In each layer of rubber, the temperature observed near the steel is lower than that inside the rubber. In the layers near the flanges, the temperature becomes much lower due to the heat transfer from rubber to the steel flanges without the heat insulated boundary conditions, as described in Section 5.

Relation between the sum of the measured vertical load, which is applied to the control node, and lateral displacement is shown in Figure 15. Figures 16(a) and 16(b) compare the load-displacement curves obtained by the tests and the analyses for the 1st and 2nd cycles of the 1st set and the 5th cycle of the 6th set. Temperature dependences of the material parameters are not taken into account in Figure 16(a), while they are considered in Figure 16(b). As seen from the figures, the energy consumption for the 1st cycle of the 1st set obtained by the test is much larger than that for the other cycles, and this behavior of unscragged rubber is not reproduced by the analysis. The test result for this cycle is not used in the parameter identification described in Section 3.5. The maximum load obtained by the analysis is slightly smaller than that obtained by the test, although the load-displacement curve obtained by the analysis using the rectangular coupon model agrees well with the result of the test described in Section 3.5 because the parameter identification is conducted using the coupon model. As shown in Figure 16, the absolute values of the maximum and the minimum loads obtained by the test decrease as the number of cycles increases and the temperature rises due to the dissipated energy. The analysis result shown in Figure 16(a) does not simulate this phenomenon; that is, the shape of the load-displacement curve does not change because the temperature dependence of the material parameters is not considered. In contrast, the decrease of the absolute values of the maximum and the minimum loads is simulated in the analysis result in Figure 16(b) when the temperature dependence is considered. The area of the hysteresis loop, which corresponds to energy dissipation, and the stiffness of the entire HDRB are simulated; accordingly, the temperature rise in the rubber is also simulated.

Figures 17 (a)-(d) compares temperature histories at points A1, B1, C2, and C3, respectively, as obtained by the test and the analysis. Note that initial temperatures at different points, which are indicated in the legends by the symbol T0, are different in the test because the tests for various loading cases were conducted previously and the rubber did not cool down completely. For the analyses, the initial temperature in the analyses is assumed to be 30 °C at all integration points of the finite elements. To compare the analysis and test results, the temperature rise from the initial state is drawn in Figure 17. Note that the one-directional loading was conducted after the elliptical loading test shown in Section 6.2, and the thermocouple at point C3 had trouble during the test.

Figure 18 compares the external work obtained by the test and the analysis. The dissipated energy, the elastic energy, and the sum of these two energies are also shown for the analysis in Figure 18. As seen from the figure, the elastic energy also accumulates as the number of cycles increases, which means residual stress accumulates in the rubber. The sums of the dissipated energy and the elastic energy are almost the same as the external work value. However, they do not agree exactly because the dissipated energy is calculated approximately; that is, some conditions, such as the change of the material parameters due to the temperature rise in an increment, are not considered.

Figure 19 compares the equivalent damping factors obtained by the test, the analyses, and the empirical formula in each cycle, and Figure 20 compares the equivalent stiffnesses obtained by the test, the analyses, and the empirical formula in each cycle. The temperature at point C2 is used for the empirical formulae because it was used as the representative temperature of the HDRB in making the formulae. The slopes of the results using the formulae are almost the same as those of the results of the test and the analysis.

6.2 Results for two-directional elliptical loading and earthquake loading

Figure 21 shows the deformation and contours of the equivalent stress at a time step of the last (5th) cycle of

the 6th set of loading when the lateral displacement at the control node is maximum. Figure 22 shows a cross-sectional view of temperature contours at the last time step. Figures 23(a) and 23(b) compare the load-displacement curves obtained by the test and the analysis in the longer and shorter axis directions, respectively, for the 1st cycle of the 1st set, the 5th cycle of the 3rd set, and the 5th cycle of the 6th set. The temperature dependences of the material parameters are taken into account in the analysis. In the result of the test, unscragged rubber behavior can be observed in the hysteresis of the first loading cycle. There might be partial recovery to an unscragged state, even in the short interval of 30 min after the previous test. However, this phenomenon is not reproduced by the analysis. As seen from the figures, the loads at the maximum and minimum displacements obtained by the test and the analysis almost agree. However, the areas of the hysteresis loops, that is, the energy consumption, obtained by the analysis are much smaller than those obtained by the test even after the first loading cycle. The differences are much larger in the shorter axis direction.

Figures 24(a)–(d) show the temperature histories obtained by the test and the analyses at points A1, B1, C2, and C3, respectively, indicated in Figure 2. Figure 25 compares the external work obtained by the test and the analysis. The dissipated energy, the elastic energy, and the sum of these two energies are also shown for the analysis. The percentage of the elastic energy is larger than that for the one-directional loading case, which means that the residual stress is larger in the elliptical loading case. It can be seen from these figures that the analysis result underestimates the dissipated energy, and accordingly, leads to a temperature rise smaller than that for the test result. The results indicate that the material parameter identification using only the test results for one-directional loading is not sufficient. In the elliptical loading, the loading speed in the longer axis direction is similar to that in the one-directional loading. In the shorter axis direction, however, the loading speed is much smaller. The results suggest that the contribution of the viscoelasticity that depends on the velocity should be larger than the parameter values used in the present study.

An analysis is also conducted for two-directional earthquake loading. For investigating the behaviors of the HDRBs, it is reasonable to assume that the bearing is subjected to motion with a dominant period of around 4 s, which is the fundamental natural period of typical base-isolated buildings. Figure 26 compares load-displacement curves for the earthquake loading case in the Y direction. Although a peak at a period of 4 s, which is the same as the period of the one-directional loading, can be found in the acceleration response spectrum of the earthquake wave, the loading speeds in the earthquake loading are different from those in the one-directional loading. Energy dissipation calculated by the analysis is smaller than that in the test.

6.3 Computation time

The present analyses use a supercomputer at NIED having 400 computation nodes. Each node has two Intel Xeon E5 2697 v2 CPUs. Each CPU has 12 cores, and thus each node has 24 cores. In the analyses, 64 cores of three nodes are used for 64 MPI processes in parallel. As an asymmetric linear solver for the implicit finite element analysis, the GPBi-CG method is used with the combined Coarse Grid-based Conjugate Gradient and SOR preconditioner (CGCG2_SOR) that is implemented in ADVENTURECluster. Computation times for the case of the one-directional loading considering the temperature dependence of the material parameters and the case of the elliptical loading are 150.3 h and 299.4 h, respectively.

7. Concluding remarks

A framework for coupled structural and heat conduction FE analysis has been developed for HDRBs. Full-scale tests of an HDRB using the shaking table at E-Defense are simulated using the coupled structural and transient heat conduction FE analysis. The HDRB is modeled as a mesh of hexahedral solid elements. The temperature rise due to the dissipated energy of inelastic deformation of the HDRB by cyclic loading is simulated by the FE structural analysis, and the temperature distribution is computed by the FE heat conduction analysis. The temperature dependence of material parameters is considered in the FE structural analysis.

The high damping rubber is modeled using an overlaid visco-hyperelastic and elastic-plastic constitutive model. A material parameter identification tool combining simulated annealing and the E-Simulator is also developed. However, no cyclic coupon test was conducted for the high damping rubber used in the E-Defense tests. Therefore, material parameters are identified approximately as follows:

(1) Material parameters at approximately 30 °C are identified using the results of the one-directional loading test of the HDRB.

(2) Temperature dependences of the material parameters are determined using the empirical formulae for the equivalent stiffness and the equivalent damping, which were derived from the results of the E-Defense tests and its preliminary test in the previous study [1].

(3) The temperature dependence of the equivalent damping is represented only by taking into account the temperature dependence of the yield stress, although this assumption is not generalizable.

(4) Behavior of the HDRB in the unscragged state is not taken into account.

Although the material model with the material parameters used in the present study has a number of limitations, the numerical examples show that the framework of the coupled structural and heat conduction FE

analysis developed in this study works well as follows:
(1) The one-directional loading case is simulated successfully because the material parameters are identified using the results of the one-directional loading case, and hysteresis at each temperature can be reproduced by the analysis. The load-displacement curves, temperature rise, and dissipated energy obtained by the coupled analysis show good agreements with the test results except for the first cycle in an unscragged state. The coupling effect of the mechanical and thermal behaviors are clearly shown.
(2) Decreases of the equivalent stiffness and the equivalent damping factors for the entire structure of the HDRB due to temperature rise can be simulated.

However, the approximate analysis conditions in the preset study have several limitations:
(1) Two-directional loading cases are not simulated accurately because the material parameters are identified using only the test results for one-directional loading. The parameters for the viscoelastic model should be identified using the results of coupon tests at various loading speeds.
(2) The simple method for considering the temperature dependence of the dissipated energy cannot be applied to cases with temperatures higher than 60 °C.
(3) The significance of the coupled structural and heat conduction FE analysis of HDRBs cannot be demonstrated by the present numerical results because the number of cycles of loading applied in the present numerical examples is only 30, and the amount of heat generation is small.

The temperature rise in the HDRB subjected to the predicted Great Nankai Trough Earthquakes is estimated to be approximately 70–80 °C The final target of our research is to simulate a base-isolated structure using HDRBs subjected to these earthquake excitations. Because the framework of the coupled analysis has been developed, the authors are now planning to conduct cyclic coupon test of the rubber. Finally, the structural performance of various kinds of HDRBs considering the coupling effect will be evaluated without component tests but with FE analyses based only on the results of material coupon tests.

Acknowledgements This study is a part of E-Defense Seismic Experimental Study and E-Simulator Development Project at the National Research Institute for Earth Science and Disaster Resilience (NIED). The authors acknowledge the valuable contribution from the committee members and the financial support of NIED. The data from the full-scale HDRB test (the E-Defense tests) were obtained from the Archives of Shaking-table Experimentation dataBase and Information (ASEBI) [42], operated by NIED. Dr. Takuzo Yamashita at NIED conducted part of the post-processing of analysis and test results. Useful advice on the nonlinear formulations used in ADVENTURECluster and support by Dr. Tomonobu Ohyama and members of the ADVC division at Allied Engineering Corporation are gratefully acknowledged. The present study was also supported by the Japan Society for the Promotion of Science, KAKENHI grants 19H02286 and 16K05046.

References

1. Yamamoto S, Nakanishi K, Kakinuma T, Kitamura H, Takayama M, Sato E, Iiba M. Study on Multi-cyclic Characteristics of Devices for Seismic Isolation against Long Period Earthquake Motions (Multi-cyclic Loading Experiment on Full-scale High-damping Rubber Bearing). In: Proceedings of the 13th World Conference on Seismic Isolation, Energy Dissipation and Active Vibration Control of Structures, Sendai, Japan, 2013.
2. Ohsaki M, Miyamura T, Kohiyama M, Yamashita T, Yamamoto M, Nakamura N. Finite-element analysis of laminated rubber bearing of building frame under seismic excitation. *Earthquake Eng. Struct Dyn.* 2015; **44**:1881–1898.
3. Allied Engineering Corporation. https://www.alde.co.jp/en/service/advc/ [February 9, 2021].
4. Akiba H *et al*. Large Scale Drop Impact Analysis of Mobile Phone Using ADVC on Blue Gene/L. In: Proceedings of the International Conference for High Performance Computing Networking and Storage (SC06), Tampa, FL, 2006; Paper No. 46.
5. Ohsaki M, Miyamura T, Kohiyama M, Hori M, Noguchi H, Akiba H, Kajiwara K, Ine T. High-precision finite element analysis of elastoplastic dynamic responses of super-highrise steel frames. *Earthquake Engineering and Structural Dynamics* 2009; **38**(5):635–654.
6. Miyamura T, Yamashita T, Akiba H, Ohsaki M. Dynamic FE simulation of four-story steel frame modeled by solid elements and its validation using results of full-scale shake-table test. *Earthquake Eng. Struct. Dyn*. 2015; **44**:1449–1469.
7. Iizuka M. A macroscopic model for predicting large-deformation behaviors of laminated rubber bearings. *Engineering Structures* 2000; **22**:323–334.
8. Kelly JM, Konstantinidis DA. *Mechanics of Rubber Bearings for Seismic and Vibration Isolation* 2011, John Wiley & Sons.
9. Constantinou MC, Whittaker AS, Kalpakidis Y, Fenz DM, Warn GP. Performance of seismic isolation hardware under service and seismic loading. *MCEER technical report, University at Buffalo* 2007, MCEER-07-0012.

10. Ogden RW. Large deformation isotropic elasticity, on the correlation of the theory and experiment for incompressible rubberlike solids. *Proceedings of Royal Society of London Series A* 1972; **328**:567–583.
11. de Souza Neto, EA, Perić, D, Owen, DRJ. *Computational Methods for Plasticity: Theory and Applications*. New York: John Wiley & Sons; 2008. Section 13.2.1.
12. Matsuda A. Evaluation for mechanical properties of laminated rubber bearings using finite element analysis. *Journal of Pressure Vessel Technology* 2004; **126**(2):134–140.
13. Matsuda A. Finite element analysis of high damping rubber bearings using nonlinear viscoelastic model. *Transaction of Japan Society of Mechanical Engineering, Series A* 2002; **68**(669):17-24. (in Japanese)
14. Kalfas KN, Mitoulis SA, Katakalos K. Numerical study on the response of steel-laminated elastomeric bearings subjected to variable axial loads and development of local tensile stresses. *Engineering Structures* 2017; **134**:346–357.
15. Moghadam SR, Konstantinidis D. Finite element study of the effect of support rotation on the horizontal behavior of elastomeric bearings. *Composite Structures* 2017; **163**:474–490.
16. Abe M, Yoshida J, Fujino Y. Multiaxial behaviors of laminated rubber bearings and their modeling, II: Modeling, *Journal of Structural Engineering* (ASCE) 2004; **130**(8): 1133–1144.
17. Yamamoto M, Minewaki S, Yoneda H, Higashino M. Nonlinear behavior of high-damping rubber bearings under horizontal bidirectional loading: full-scale tests and analytical modeling. *Earthquake Engineering and Structural Dynamics* 2012; **41**(13):1845–1860.
18. Yoshida J, Sugiyama T. A hyperelastic visco-elasto-plastic damage model for rubber-like solids including strain-dependency of hyperelastic loops. *J. Applied Mechanics*, *JSCE* 2015; **71**(1):14–33. (in Japanese)
19. Yuan Y, Wei W, Tan P, Igarashi A, Zhu H, Iemura H, Aoki T. A rate-dependent constitutive model of high damping rubber bearings: Modeling and experimental verification. *Earthquake Engineering and Structural Dynamics* 2016; **45**:1875–1892.
20. Mordini A, Stauss A. An innovative earthquake isolation system using fibre reinforced rubber bearings. *Engineering Structures* 2008; **33**:2239–2751.
21. Das A, Dutta A, Deb SK. Performance of fiber-reinforced elastomeric base isolators under cyclic excitation. *Structural Control and Health Monitoring* 2015; **22**(2): 197–220.
22. Gracia LA, Liarte E, Pelegay JL, Calvo B. Finite element simulation of the hysteretic behavior of an industrial rubber: Application to design of rubber components. *Finite Elements in Analysis and Design* 2010; **46**(4):357–368.
23. Miehe C, Keck J. Superimposed finite elastic–viscoelastic–plastoelastic stress response with damage in filled rubbery polymers: Experiments, modelling and algorithmic Implementation. *Journal of Mechanics and Physics of Solids* 2000; **48**:323–365.
24. Simo JC. On a fully three-dimensional finite-strain viscoelastic damage model: Formulation and computational aspects. *Computer Methods in Applied Mechanics and Engineering* 1987; **60**(2):153–173.
25. Kalpakidis IV, Constantinou MC. Effects of heating on the behavior of lead-rubber bearings, I: Theory. *J. Structural Engineering*, *ASCE* 2009; **135**(12):1440–1449.
26. Kalpakidis IV, Constantinou MC. Effects of heating on the behavior of lead-rubber bearings, II: Verification and theory. *J. Structural Engineering*, *ASCE* 2009; **135**(12):1450–1461.
27. Kalpakidis IV, Constantinou MC, Whittaker AS. Modeling strength degradation in lead–rubber bearings under earthquake shaking. *Earthquake Engineering and Structural Dynamics* 2010; **39**:1533–1549.
28. Cardone D, Gesualdi G, Nigro D. Effects of air temperature on the cyclic behavior of elastomeric seismic isolators. *Bulletin of Earthquake Engineering* 2011; **9**:1227–1225.
29. Cardone D, Gesualdi G. Experimental evaluation of the mechanical behavior of elastometric materials for seismic applications at different air temperatures. *Int. J. Mech. Sci.* 2012; **64**:127–143.
30. Kuroshima Y, Ishii K, Kikuchi M, Iiba M, Shirai K. Seismic response analysis of isolated buidings in consideration of the thermal and mechanical coupling behavior of lead rubber bearings. *Journal of Structural Engineering* (AIJ) 2017; **63B**: 231-240.
31. Yukawa M, Inaba S, Takeuchi Y, Furuhashi T, Nakamura T, Naito N. Behavior of lead rubber bearing by heat accompany multi-cyclic loading - A consideration of analysis method of heating iteration behavior by thermal energy evaluation -. *Journal of Structural and Construction Engineering* (*Transactions of AIJ*) 2018; **83**(745):385-395. (in Japanese)
32. Takenaka Y, Kondo A, Takaoka E, Hikita M, Kitamura H, Nakamura T. Experimental study on heat-mechanics interaction behavior of laminated rubber bearings. *Journal of Structural and Construction Engineering* (*Transactions of AIJ*) 2009; **74**(646):2245-2253. (in Japanese)
33. Kitamura H, Hayakawa S, Takenaka Y, Takaoka E, Murota N. Evaluation of the influence of heat-mechanics interaction behavior in high-damping rubber bearings on seismic response of base-isolated buildings. *Journal of Structural and Construction Engineering* (*Transactions of AIJ*) 2010; **75**(655): 1635-1644. (in Japanese)

34. Dhakal, YP, Suzuki, W, Kimura, T, Morikawa, N, Kunugi, T, Aoi S. Evidence of strong long-period ground motions of engineering importance for Nankai Trough plate boundary earthquakes: comparison of ground motions of two moderate-magnitude earthquakes. *Earth, Planets and Space* 2018; 70: Article number 189.
35. Project for Making Map for Predicting Long-Period Ground Motion. *Annual Report FY 2011*. R&D Division of MEXT and National Research Institute for Earth Science and Disaster Resilience; 2012. (in Japanese)
36. Clark PW. *Experimental studies of the ultimate behaviro of seismically-isolated structures*. Doctoral Dissertation, University of California, Berkley, United States, 1996.
37. Allied Engineering Corporation. *Manual of ADVENTURECluster Solver 2019 R1.0*. 2019. (in Japanese)
38. Argyris J. An excursion into large rotations. *Computer Methods in Applied Mechanics and Engineering* 1982; **32**:85-155.
39. Hisada T, Noguchi H. *Foundation and Application of Nonlinear Finite Element Method*. Tokyo: Maruzen; 1995. (in Japanese)
40. Aarts, E, Korst, J. *Simulated annealing and Boltzmann machines*, John Wiley & Sons; 1989.
41. Simo JC, Armero F. Geometrically Nonlinear Enhanced Strain Mixed Methods and the Method of Incompatible Modes, *International Journal for Numerical Methods in Engineering* 1992; 33: 1413-1449.
42. Study on the safety verification method of base isolated buildings subjected to long-period earthquake motions. ASEBI, NIED. https://www.edgrid.jp/ [February 9, 2021].

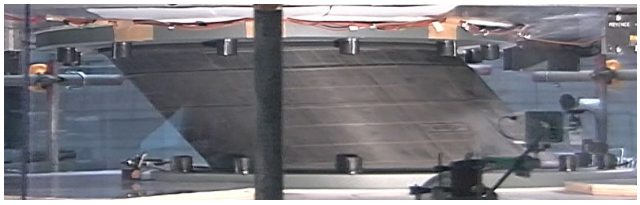

Figure 1. Laminated high damping rubber bearing (HDRB) undergoing lateral loading in the test facility.

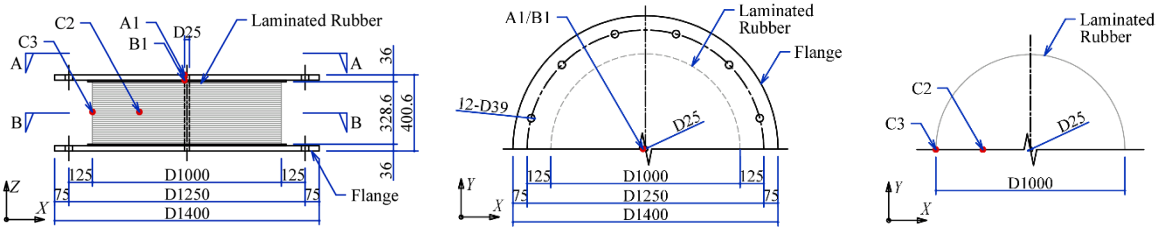

(a) Elevation (b) A-A plan (flange) (c) B-B plan (rubber)

Figure 2. Plans and section of the HDRB and locations of thermocouples that are indicated by red circles (units: mm).

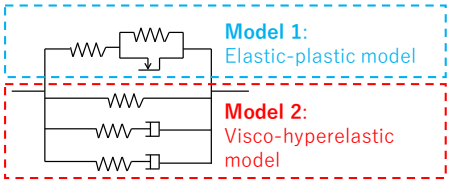

Figure 3. Overlaid visco-hyperelastic and elastic-plastic constitutive model.

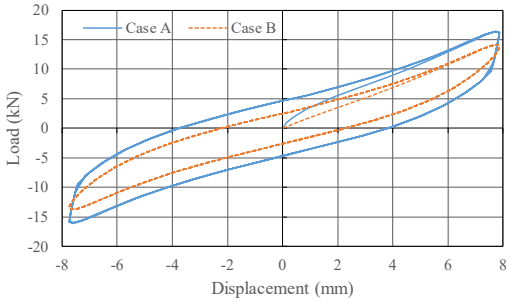

Figure 4. Load-displacement curves for different yield stresses obtained by the rectangular coupon model; the initial yield stress for Case A is given in Table 2, and that for Case B is almost zero.

Table 1. Material parameters for visco-hyperelastic rubber model at 30 °C.

Density (t/mm^3)		1.15×10^{-9}
Coefficient of thermal expansion (1/K)		2×10^{-4}
Heat conductivity (mW/mm K)		0.31
Specific heat capacity [mJ/(t K)]		1.45×10^{9}
Parameters for hyperelastic Ogden model	μ_1 (MPa)	0.19
	α_1	3.8
	μ_2 (MPa)	1.06
	α_2	1.175
	K (MPa)	3000
	β	0.3333
	γ	1.0
Parameters for Prony series in Maxwell model 1	Dimensionless elastic shear modulus g_1	0.2
	Dimensionless elastic bulk modulus k_1	0.2
	Relaxation time t_1 (s)	0.130
Parameters for Prony series in Maxwell model 2	Dimensionless elastic shear modulus g_2	0.2
	Dimensionless elastic bulk modulus k_2	0.2
	Relaxation time t_2 (s)	0.165

Table 2. Material parameters for elastic-plastic rubber model at 30 °C.

Density (t/mm^3)	1.15×10^{-9}
Young's modulus E (MPa)	20.0
Poisson's ratio	0.3
Initial yield stress (MPa)	0.2
Hardening coefficient (MPa)	2×10^{-2}
Coefficient of thermal expansion (1/K)	2×10^{-4}
Heat conductivity (mW/mm K)	0.31
Specific heat capacity [mJ/(t K)]	1.45×10^{9}

Table 3. Material parameters for steel at 30 °C.

Density (t/mm^3)	7.86×10^{-9}
Young's modulus (MPa)	2.05×10^{5}
Poisson's ratio	0.3
Yield stress (MPa)	235
Hardening coefficient (MPa)	205
Coefficient of thermal expansion (1/K)	1.17×10^{-5}
Heat conductivity (mW/mm K)	51.6
Specific heat capacity [mJ/(t K)]	4.73×10^{8}

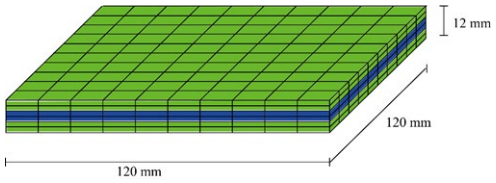

Figure 5. Mesh of the rectangular coupon model.

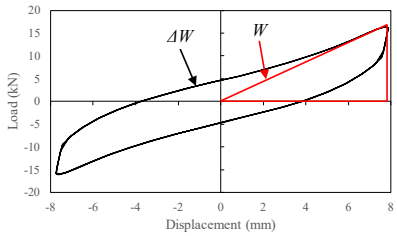

Figure 6. Dissipated energy (energy consumption) and the maximum potential energy.

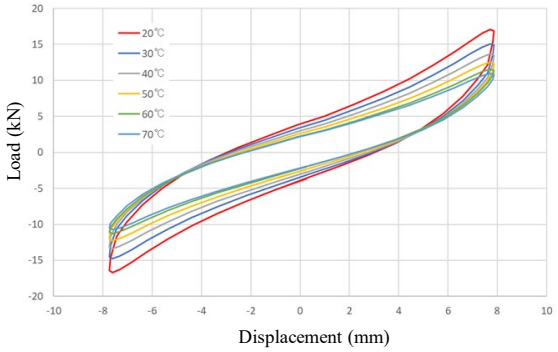

Figure 7. Hysteresis loops in the load-displacement curves for different temperatures.

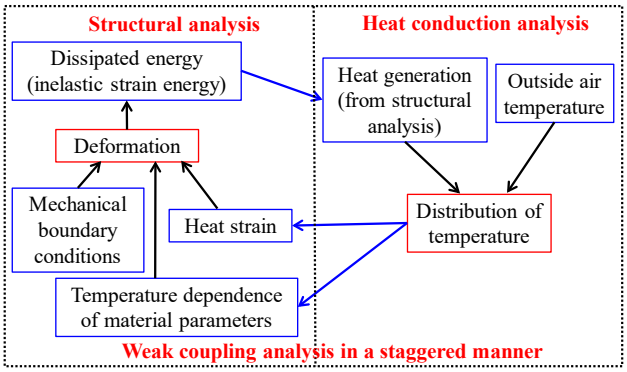

Figure 8. Schematic flow of the combined structural and heat conduction analysis.

Table 4. Comparison between equivalent damping factors obtained by the FE analyses and the empirical equation for different temperatures.

Temperature (°C)	Maximum strain energy W (N mm)	Dissipated energy ΔW (N mm)	Equivalent damping factor $h_{eq} = \Delta W / (4\pi W)$	Equivalent damping factor obtained by Eq. (39)	Difference (%)
20	6.7×10^4	1.1×10^5	0.126	0.130*	3.7
30	5.9×10^4	9.1×10^4	0.122	0.122	—
40	5.4×10^4	7.8×10^4	0.115	0.113	1.6
50	4.9×10^4	6.6×10^4	0.106	0.105	1.4
55	4.7×10^4	6.0×10^4	0.101	0.101	0.5
60	4.5×10^4	5.4×10^4	0.0953	0.0963	1.1
70	4.3×10^4	5.2×10^4	0.0961	0.0879	9.4

* $h_{eq}(20) = h_{eq}(30) / C_H(30) = 0.122 / C_H(30) = 0.130$

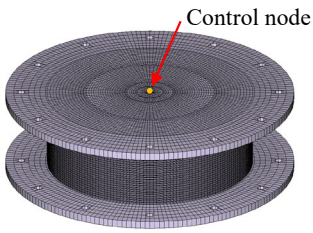

(a) Entire view

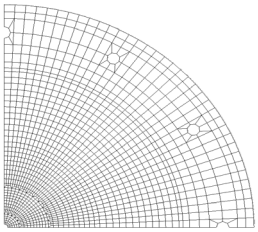

(b) Plan view (quarter portion)

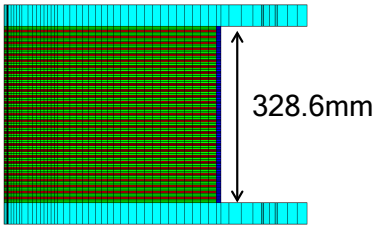

(c) Elevation view

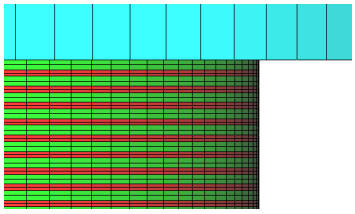

(d) Close-up of elevation view

Figure 9. Mesh of the bearing.

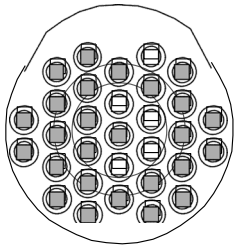

(a) Locations of load cells

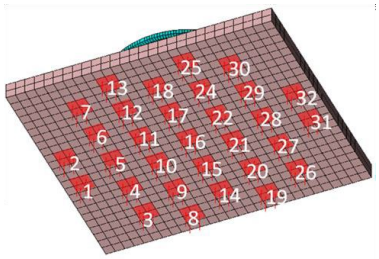

(b) Boundary conditions for the load cell model; each load cell is modeled as a set of four segments shown in red on the surface patch

Figure 10. Boundary conditions for the load cell model.

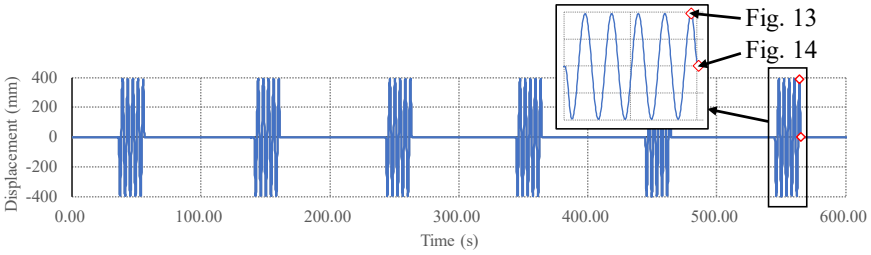

Figure 11. History of measured lateral displacement that is assigned to the control node and prescribed as the time-dependent nodal displacement; the control node is shown in Fig. 9(a).

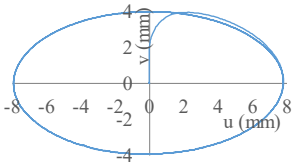

Figure 12 Elliptical orbit for two-directional loading.

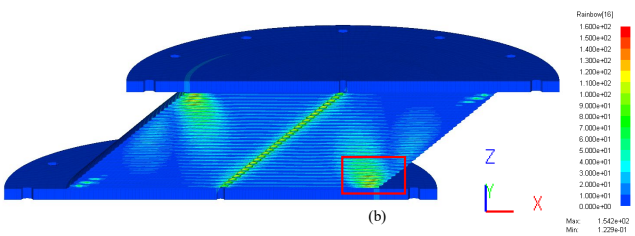

(a) Entire view

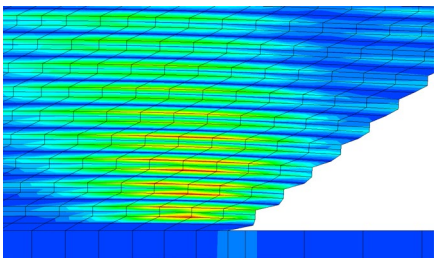

(b) Close-up view of region indicated by red rectangle in panel (a)

Figure 13. Deformation and contours of equivalent stress at one time step of the 5th loading cycle of the 6th set of loading, when the lateral displacement is maximum; this is a one-directional loading case for the time step shown in Fig. 11.

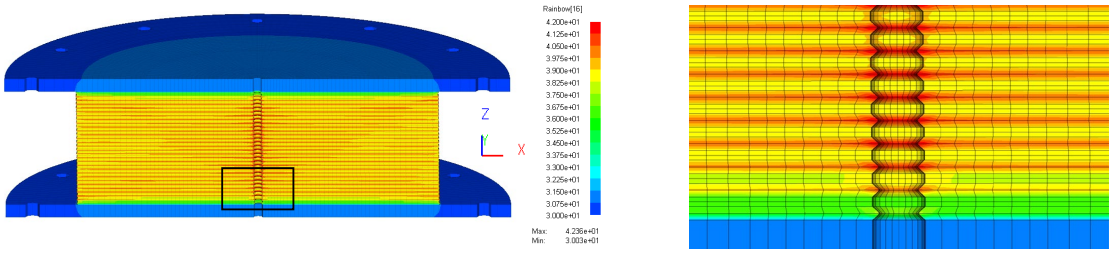

(a) Entire view

(b) Close-up view for the region indicated by black rectangle in panel (a)

Figure 14. Cross-sectional view of contour of temperature at the last time step of the 6th loading set; this is a one-directional loading case for the time step shown in Fig. 11.

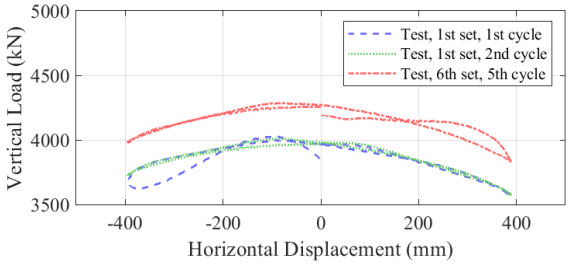

Figure 15. Relation between the sum of the measured vertical load and lateral displacement for the 1st and 6th loading sets of one-directional loading.

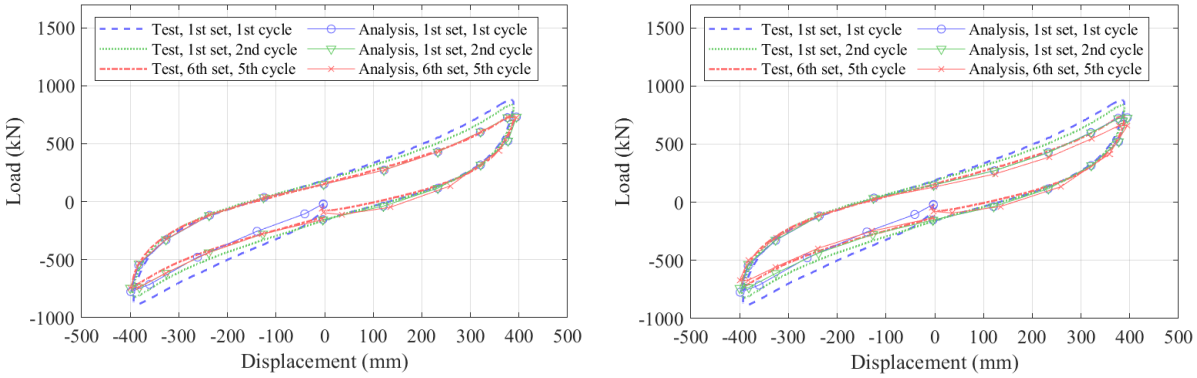

(a) Without consideration of temperature dependence of material parameters

(b) With consideration of temperature dependence of material parameters

Figure 16. Load-displacement curves for the 1st and 6th loading sets of one-directional loading case.

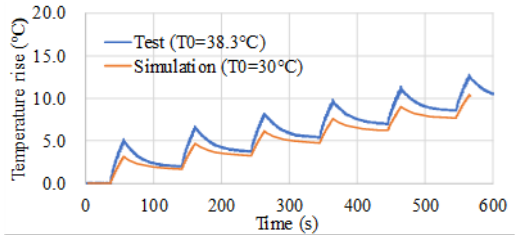

(a) Point C2 (inside rubber)

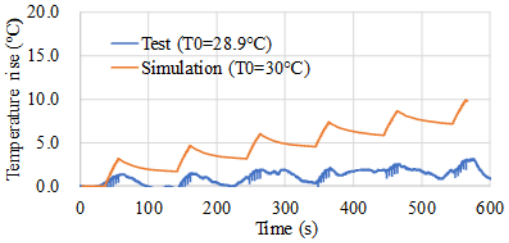

(b) Point C3 (inside rubber) (this thermocouple may be broken)

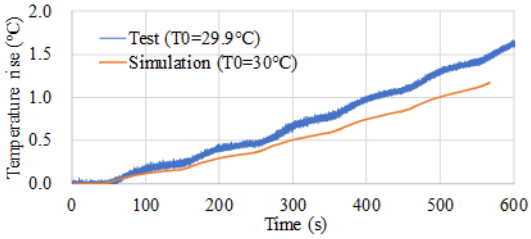

(c) Point A1 (upper face of upper flange)

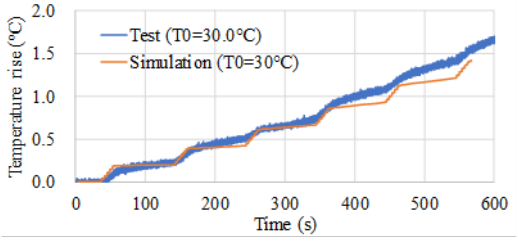

(d) Point B1 (lower face of upper flange)

Figure 17. Temperature histories for one-directional loading; T0 indicates temperature at time 0.

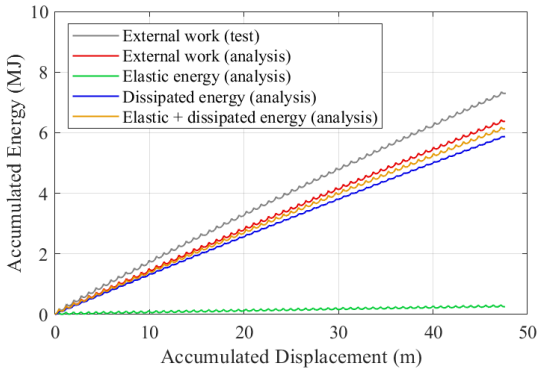

Figure 18. Accumulated dissipated energy for one-directional loading with consideration of temperature dependence of material parameters.

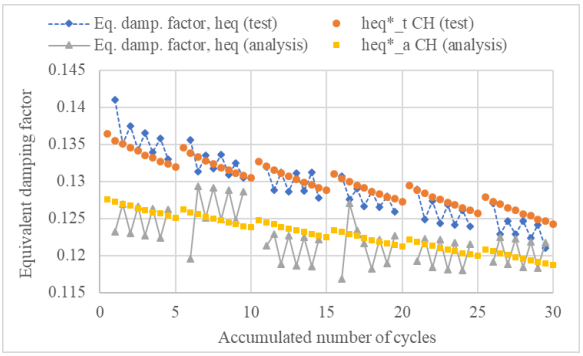

heq*_t CH= $h_{eq}(40.4)C_H(T)/C_H(40.4)$ (h_{eq} is obtained by test)

heq*_a CH= $h_{eq}(40.4)C_H(T)/C_H(40.4)$ (h_{eq} is obtained by the analysis)

Figure 19. Comparison of equivalent damping factors obtained by test, analysis, and empirical formula for one-directional loading case; the temperature at point C2 is used for the empirical formula.

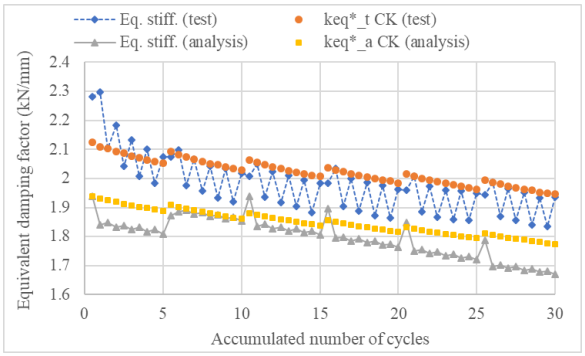

keq*_t CH= $k_{eq}(40.4)C_K(T)/C_K(40.4)$ (k_{eq} is the equivalent stiffness obtained by test)

keq*_a CH= $k_{eq}(40.4)C_K(T)/C_K(40.4)$ (k_{eq} is the equivalent stiffness obtained by the analysis)

Figure 20. Comparison of equivalent stiffnesses obtained by test, analysis, and empirical formula for one-directional loading case; the temperature at point C2 is used for the empirical formula.

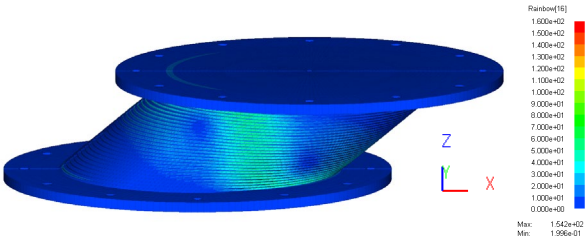

Figure 21. Deformation and contours of equivalent stress at one time step of the 5th loading cycle of the 6th set, when the lateral displacement is maximum under elliptical loading.

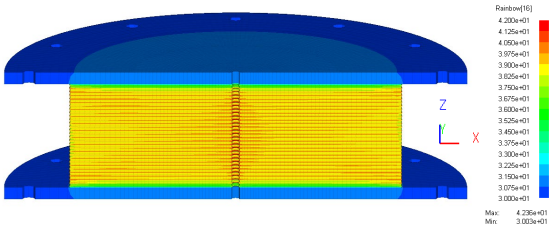

Figure 22. Cross sectional view of temperature contours at the last time step of the 6th loading set under elliptical loading.

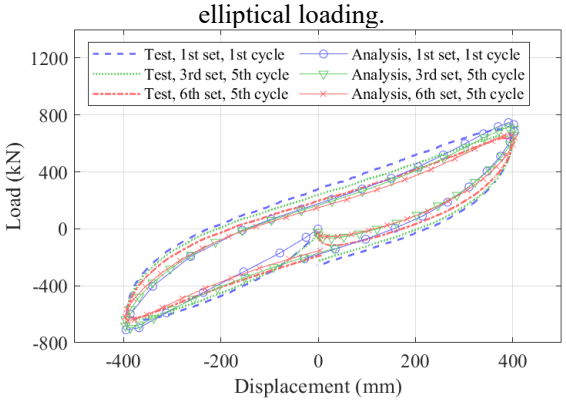

(a) Longer axial direction

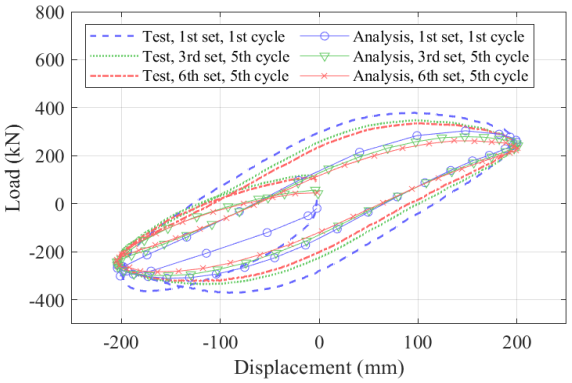

(b) Shorter axial direction

Figure 23. Load-displacement curves of elliptical loading case with consideration of temperature dependence of material parameters.

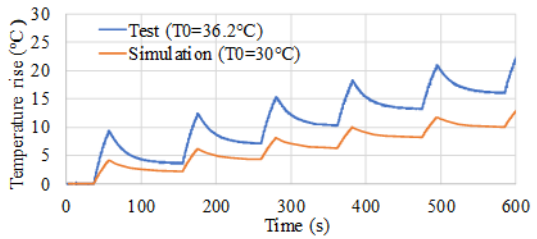

(a) Point C2 (inside rubber)

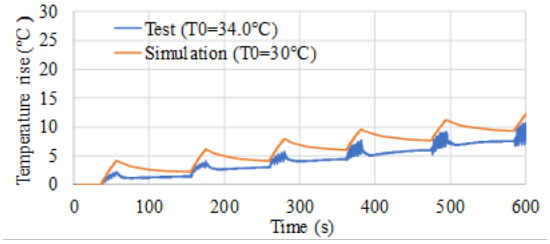

(b) Point C3 (inside rubber)

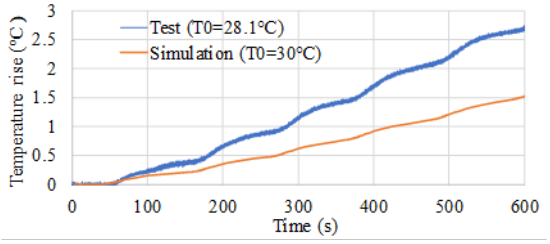

(c) Point A1 (upper face of upper flange)

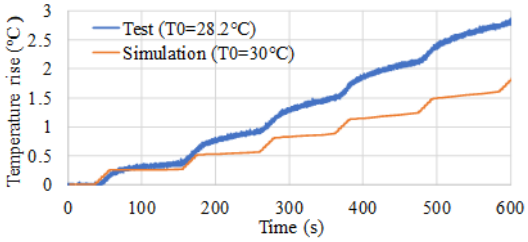

(d) Point B1 (lower face of upper flange)

Figure 24. Temperature histories of elliptical loading case with consideration of temperature dependence of material parameters; T0 indicates temperature at time 0.

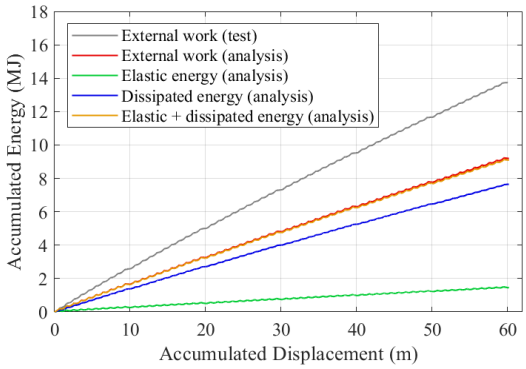

Figure 25. Accumulated dissipated energy of elliptical loading case.

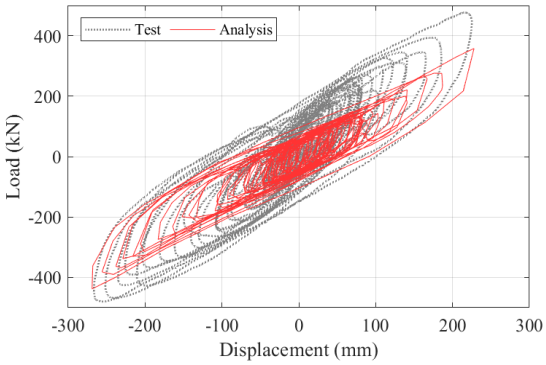

Figure 26. Load-displacement curves of the earthquake loading case (Y direction) with consideration of temperature dependence of material parameters.